Research Article | Vol. 29, No. 14 / 5 July 2021 / Optics Express 22376
Optics EXPRESS

# Photonic crystal light trapping for photocatalysis

XIWEN ZHANG[1,2] AND SAJEEV JOHN[1,3]

[1]Department of Physics, University of Toronto, 60 Saint George Street, Toronto, Ontario M5S 1A7, Canada
[2]xiwen@mail.ustc.edu.cn
[3]john@physics.utoronto.ca

**Abstract:** The Achilles heel of wide-band photocatalysts such as $TiO_2$ is the insufficient photogeneration in the visible range under sunlight. This has been a longstanding impediment to large-scale, real-world deployment of titania-based photocatalysis applications. Instead of traditional band engineering through heavy-doping, we suggest enhancing photocatalytic efficiency of lightly-doped $TiO_2$ using photonic crystal (PC) structures. This strongly increases solar photogeneration through novel wave-interference-based light trapping. Four photocatalyst structures — simple cubic woodpile (wdp), square lattice nanorod (nrPC), slanted conical-pore (scPore), and face-centered cubic inverse opal (invop) — are optimized and compared for light harvesting in the sub- and above-gap (282 to 550 nm) regions of weakly absorbing $TiO_2$, with the imaginary part of the dielectric constant 0.01 in the visible range. The optimized lattice constants for the first three, and opal center-to-center distance for invop, are ~300 - 350 nm. For fixed PC thickness, the ranking of visible light harvesting capability is: scPore > wdp ~ nrPC > invop. The scPore PC deposited on highly reflective substrate is ideal for photocatalysis given its combination of enhanced light trapping and superior charge transport.



## 1. Introduction

Photocatalysis has been widely studied since the early 20th century and has become a recent research focus due to global problems of energy harvesting and storage, removal of environmental pollutants, and public health. $TiO_2$ draws broad interest as a functional material [1,2] due to its favorable photochemical activity, physical and chemical stability, abundancy, nontoxicity, and biocompatibility. It is extensively used as white pigment, for dielectric coatings [1], sensors [3], photovoltaics [4], electrochromic devices [5], and medical implants [6]. $TiO_2$-based photocatalysis holds promise for hydrogen fuel generation by water splitting [7,8], environmental remediation [9], and biomedical germicide and drug delivery [10,11]. Improving $TiO_2$ photocatalytic efficiency is the key to real-world deployment of many applications. This involves the management of charge carriers surface redox reaction, bulk charge transport, and their photogeneration from sunlight.

The crucial step of electron-hole pair photogeneration sets a fundamental limit for the photocatalytic process. The large bandgap of $TiO_2$ in the near-UV range, critically restricts the reaction efficiency under sunlight. Essentially, only the ~ 4% UV energy of solar irradiance is effective for pristine titania-based photocatalyst, while the ~ 42% visible light energy is not involved in photocarrier generation. To solve this problem, extensive effort has been devoted to the band engineering of $TiO_2$ by introducing various intrinsic and extrinsic defect states to lower the absorption bandgap to enable visible light harvesting [1,2].

Intrinsic oxygen vacancies naturally occur in $TiO_2$ during crystal growth, as well as in samples that are electron bombarded or thermally treated (in reducing atmospheres) [12]. They account for the n-type nature of $TiO_2$, and introduce defect states commonly in the form of $Ti^{3+}$ lying ~ 1 eV below the conduction band minimum [13–15]. Although these defect states may act as electron-hole recombination centers [16,17], they can nonetheless be beneficial for enhancing photocatalytic activity in the visible range [18,19]. Extrinsic doping of some non-metal anions

#427218 https://doi.org/10.1364/OE.427218
Journal © 2021 Received 8 Apr 2021; revised 29 May 2021; accepted 7 Jun 2021; published 30 Jun 2021

Optics EXPRESS

(C, N, S, F, etc.) and a wide range of transition metal and inner transition metal cations [1,20,21], as well as the co-doping of their various combinations [22,23] and disorder-engineering (e.g., by hydrogenation) [24,25] have been applied to reduce the bandgap of $TiO_2$. While the visible light absorptivity is commonly enhanced by the extrinsic doping, the defect sites may serve as charge carriers trapping centers. Such defects affect the transport and recombination according to their wavefunction localization, details of associated intrinsic defects and surface and bulk disorders [1,26]. Whether this deteriorates or improves the photocatalytic activity depends on the detailed doping strategies [22,23,27] and dopant concentrations and distributions [1,20,28,29].

Dye photosensitization, quantum dots and noble metal nanostructures have also been applied to extend the photocatalytic reactivity to longer wavelength region [21]. For example, gold nanoparticles [30] and gold nanorods [31] have been integrated with $TiO_2$, to provide localized surface plasmon resonances in the visible and near infrared spectral ranges [32]. After absorption of visible light, photogenerated hot electrons are injected from the metal particles to $TiO_2$ [33–36] with efficiency $\sim$ 20% - 50% for plasmonic on resonance excitation [37]. Although the mechanism of the surface plasmon enhancement of the photocatalytic activity is not fully understood [21,38], the large inherent absorption loss in the metal likely curtails further improvement of the reaction efficiency.

A completely different route of increasing the light absorptivity in the sub-gap region and/or charge carrier transport is to strategically modify the larger scale morphology of the $TiO_2$ photocatalyst. Two types of $TiO_2$ photocatalyst morphologies have been widely adopted in experiments, namely, porous structures and nanowires. The advantage of these architectures lies in the ample surface area for chemisorption of reactants and straightforward carrier diffusion path for transport, respectively. The corresponding light harvesting, however, primarily relies on enhanced random scattering and long physical thickness (nanowire length). When these structures are periodically ordered (i.e., inverse opal and nanorod array as discussed in this work), optical Bloch modes emerge and a new light harvesting mechanism is enabled by light-trapping in photonic crystals (PC) [39]. Over the past decade, considerable literature has been devoted to enhancing the photocatalytic efficiency using PC photocatalysts [40,41] (see also references in [42]). Appropriate PC architectures significantly improve the light absorptivity [43] without the degradation of bulk transport. Moreover, they offer potential synergies with other techniques for enhancing photocatalytic activity. For example, $TiO_2$ PCs have been loaded with noble metal nanoparticles [44,45] and sensitized with quantum dots [46].

Despite experimental effort devoted to PC photocatalysts over the past 15 years [42], there has been limited quantitative theoretical guidance provided [47,48]. Most research has concentrated on opal and inverse opal structures. In these opal and inverse opal structures, light trapping for photocatalysis has been focused mainly on the narrow-band slow-light modes surrounding the fundamental stop gap. Very recently it was shown that the higher-order slow-light modes of inverse opals provide much better light trapping capability [49]. Given the complexity of multiple processes involved in photocatalysis, a theoretical roadmap of PC photocatalyst structures is invaluable for exploiting the full potential of photonic crystal light trapping and harvesting.

In this paper, we optimize and compare light trapping in the spectral region of $\lambda \in [282, 550]$ nm of four types of $TiO_2$ PCs: simple cubic woodpile (wdp), square lattice nanorod (nrPC), square lattice slanted conical-pore (scPore), and face-centered cubic inverse opal (invop) on both glass and highly reflective substrates. The most efficacious photonic bands of the invop PC are from 5th to 15th [49], instead of the widely studied fundamental stop gap bandedge modes. These higher-order, slow-light photonic bands are placed into the visible light region of $\lambda \in [400, 550]$ nm when the opal center-to-center distance is $\sim$ 350 nm. As the realization of these optimized photonic bands of invop requires stringent quality control in fabrication, we discuss an alternative wdp PC that can be fabricated layer-by-layer with more easily achieved precision [43,50]. The most efficacious photonic bands of the wdp PC are from 8th to 20th.

Optics EXPRESS

These bands are placed into $\lambda \in [400, 550]$ nm by choosing the lattice constant $a \sim 350$ nm and $TiO_2$ filling fraction of 50%. With only 4 layers of woodpile logs (2 unit cells), and assuming the imaginary part of the dielectric constant is 0.01 in the visible light region, this PC demonstrates $\sim 5$ times enhancement of maximum achievable photocurrent density (MAPD) compared with a planar film with the same volume of $TiO_2$. Since the large-scale implementation of high-quality wdp PC may be expensive, we also consider square lattice nanorod and slanted conical-pore PCs. These latter two structures are optimized for solar light trapping by choosing a lattice constant $\sim$ 300 - 350 nm. Although $TiO_2$ nanowires have been widely used for photocatalysis, the $TiO_2$ nrPC remains unexplored. The most efficacious two-dimensional (2D) photonic bands of the nrPC are from 6th to 12th. These bands are placed into $\lambda \in [400, 550]$ nm by choosing the lattice constant $a \sim 300$ nm and large nanorod diameter ($\gtrsim a/2$). The optimized scPore PC has cone apexes vertically below the edge of the cone bases, with base diameter equal to or 1.15 times the lattice constant. It traps light more effectively than the nrPC, without compromising the transport advantage. Comparing all four types of PCs, the scPore structure demonstrates the best sunlight harvesting for a given PC thickness, and also facilitates excellent charge carrier collection.

## 2. Optical models of $TiO_2$ and figures of merit of PCs

We consider anatase $TiO_2$ photocatalyst lightly doped with intrinsic oxygen vacancies [19] or extrinsic metal and nonmetal dopants. Such light doping is assumed to result in a weak sub-gap absorptivity without introducing excess recombination centers for photogenerated electrons and holes. The polymorph of anatase is chosen because of its higher photocatalytic activity than rutile [51]. Optical properties of $TiO_2$ thin films vary significantly with synthesis methods, deposition conditions and sample morphologies due to the differences in void fractions, unintentional intrinsic defects [52], and surface conditions [53]. Two different dielectric models, Model I and II, are considered in this work to reveal the influence of fundamental material properties.

In Model I we assume a dispersionless dielectric function $\varepsilon = \varepsilon' + i\varepsilon''$, where $\varepsilon'$ and $\varepsilon''$ are its real and imaginary parts, for the discussion of visible light harvesting in $TiO_2$ sub-gap region of $\lambda \in [400, 550]$ nm spectral range. The real part is $\varepsilon' = 5.06$ and the imaginary part is $\varepsilon'' = 0.001$ or 0.01, corresponding to pristine or lightly-doped polycrystalline anatase, respectively [43]. This imaginary part of the dielectric constant is appended to "Model I" to specify the optical model being used. For example, the pristine $TiO_2$ with $\varepsilon = 5.06 + 0.001i$ in Model I is denoted as "Model I.001". Although the extinction coefficient of $TiO_2$ is small in this sub-gap region, more solar photons are available for electron-hole pair generation than in the UV range above the electronic band gap. For hypothetical, complete absorption of incident sunlight, the MAPD [see Eq. (2) for the definition] is 1.35 mA cm$^{-2}$ for $\lambda \in [300, 400]$ nm and 8.32 mA cm$^{-2}$ for $\lambda \in [400, 550]$ nm. It is primarily the sub-gap visible light absorptivity that determines the efficiency of sunlight harvesting in lightly doped $TiO_2$. Model I also enables the scaling of Maxwell's equations with a frequency-independent dielectric constant [49]. Conclusions drawn from Model I can be generalized by rescaling the PC lattice constant and the wavelength range by a factor of $s$. Provided that $0.87 \lesssim s \lesssim 1.3$, Model I remains in the sub-gap region of $TiO_2$.

In Model II, we include the material dispersion of $TiO_2$ based on experimental data for single-crystal anatase [54]. Optical properties of single-crystal anatase were measured in different experiments [54–57], reporting an electronic bandgap around 3.5 eV [55,56]. A recent experiment measured an indirect bandgap of 3.47 eV and direct bandgap of 3.97 eV for bulk, single-crystal anatase at the temperature 20 K [57]. The polycrystalline anatase dielectric function used in our simulation is assumed to be the weighted average of the dielectric functions for light polarizations along and perpendicular to the optical axis of single crystalline anatase. The imaginary parts of the dielectric function in Ref. [54], however, are not available for $\lambda \gtrsim 350$ nm. In Model II, we supplement the available experimental data with a constant $\varepsilon'' = 0.01$ in the sub-gap region to model lightly doped $TiO_2$ (see Appendix A for details).

Optics EXPRESS

We discuss four different PC structures: face-centered cubic inverse opal (invop), simple cubic woodpile (wdp), square lattice nanorod PC (nrPC), and square lattice slanted conical-pore (scPore) [see Figs. 9(a), 1(a), 3(a) and 5(a), respectively]. The PCs are immobilized on a substrate of transparent fused silica glass (FS, refractive index 1.46) or highly reflective perfect mirror (MR) and immersed in aqueous environment with refractive index 1.33. We refer to the various PCs on FS (MR) substrates as "invop-FS(MR)", "wdp-FS(MR)", "nrPC-FS(MR)", and "scPore-FS(MR)", respectively. These structures are assumed to be infinite in the transverse ($x$-$y$) plane with finite numbers of layers $n_{\mathrm{L}}$ and/or heights along the natural growth or deposition direction ($z$).

The simulations of optical absorptivities, $A$, of $TiO_2$ PC structures and planar films are carried out by solving Maxwell's wave equation for $x$-polarized light (unless otherwise specified) at normal incidence, using the finite-difference time-domain (FDTD) method. The resolution for the simulation is taken to be 70 mesh grids per lattice constant.

We define the average absorptivity as the absorptivity spectrum $A(f)$, integrated over a given frequency range $[f_2, f_1]$, divided by the bandwidth:

$$A_{\mathrm{avg}} = \frac{1}{f_1 - f_2} \int_{f_2}^{f_1} A(f) df. \tag{1}$$

To evaluate photocatalytic response, we weight the optical absorptivity of the catalyst by the solar irradiance spectrum. This is expressed by the maximum achievable photocurrent density (MAPD) in a wavelength region $[\lambda_1, \lambda_2]$:

$$\mathrm{MAPD} = \frac{e}{hc} \int_{\lambda_1}^{\lambda_2} A(\lambda) I_s(\lambda) \lambda d\lambda. \tag{2}$$

Here $e$ is the electron charge, $h$ is the Planck constant (not to be confused with the PC height), $c$ is the speed of light in vacuum, and $I_s$ is the AM1.5G solar irradiance spectrum.

To enable the comparison of different PC architectures on light harvesting, both the average absorptivity and the MAPD are normalized by either the catalyst masses or the thicknesses of the PCs. The former isolates the light harvesting improvement due to the morphology of the photocatalyst for a given volume of the absorbing material. More specifically, we normalize $A_{\mathrm{avg}}$ and MAPD by that of a planar solid film with the same volume of $TiO_2$. The thickness of said film is called equivalent bulk thickness $d_{TiO_2}$. The absorptivity enhancement factor is defined as [49,58]:

$$\beta = A_{\mathrm{avg}}^{\mathrm{PC}} / A_{\mathrm{avg}}^{\mathrm{bulk}}, \tag{3}$$

and the MAPD enhancement factor is defined as:

$$\zeta = \mathrm{MAPD}^{\mathrm{PC}} / \mathrm{MAPD}^{\mathrm{bulk}}. \tag{4}$$

Here, $A_{\mathrm{avg}}^{\mathrm{PC}}$ ($\mathrm{MAPD}^{\mathrm{PC}}$) is the average absorptivity (MAPD) of a PC placed on FS or MR substrate, while $A_{\mathrm{avg}}^{\mathrm{bulk}}$ ($\mathrm{MAPD}^{\mathrm{bulk}}$) is that of a planar film of equivalent bulk thickness placed on a FS substrate (denoted as "bulk-FS"), calculated in the same spectral interval.

The second way of normalizing $A_{\mathrm{avg}}$ and MAPD is by the overall PC height $d_{\mathrm{PC}}$. A photocatalyst with large $d_{\mathrm{PC}}$ may have disadvantages because the photogenerated electrons can only migrate to a distance of $\sim 10$ $\mu$m before recombination occurs [59]. A comparison of visible light trapping by different PC structures on highly reflective perfect mirror substrates as functions of both equivalent bulk thickness, $d_{TiO_2}$, and overall PC height, $d_{\mathrm{PC}}$, is discussed in Sec. 6.

## 3. Simple cubic woodpile PC

The simple cubic woodpile (wdp) PC [Fig. 1(a)] can be fabricated by two-photon lithography [60] and polyelectrolyte ink writing [61] of templates, followed by backfilling with dielectric materials

Optics EXPRESS

via techniques such as chemical vapor deposition. Alternatively, layer-by-layer microfabrication techniques provide a precise top-down approach to fabricate high quality wdp PCs [43,50]. Specifically, a simple cubic $TiO_2$ wdp produced by such layer-by-layer technique has demonstrated strong PC light trapping effect over a broad spectrum using higher order photonic modes [43].

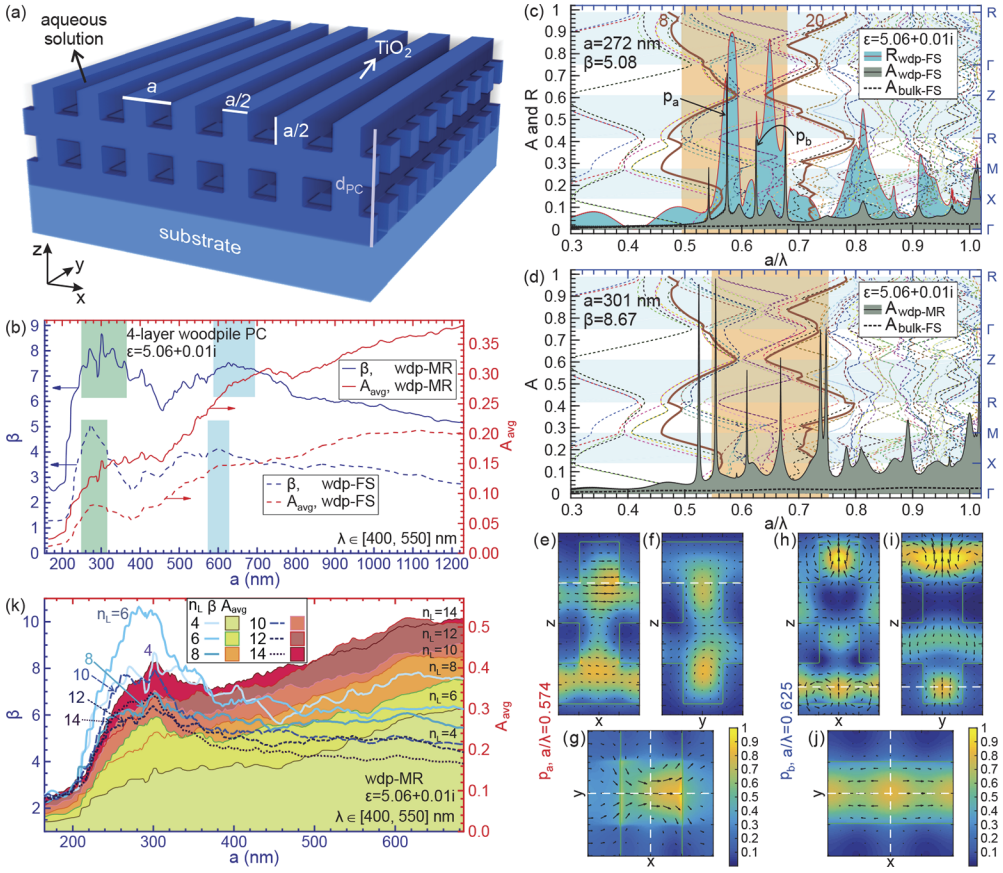


**Fig. 1.** Light trapping of $TiO_2$ simple cubic woodpile in aqueous solution for $\lambda \in [400, 550]$ nm using dispersionless dielectric Model I.01. (a) Illustration of wdp PC with lattice constant $a$ and filling fraction $F = 50\%$. (b) $A_{avg}$ and $\beta$ for wdp-FS and wdp-MR architectures, with color shades highlighting the optimized ranges of $a$. (c, d) Spectra of absorptivity $A$ and reflectivity $R$ of 4-layer (c) wdp-FS and (d) wdp-MR architectures, and that of a planar $TiO_2$ film with equivalent bulk thickness ($d_{TiO_2}$) on FS substrates. The background color dashed lines depict the band diagram of simple cubic wdp in aqueous solution. The orange shadings demark $\lambda \in [400, 550]$ nm for (c) $a = 272$ nm and (d) $a = 301$ nm, respectively, for which $\beta$ is calculated. (e-j) Distributions of electromagnetic energies (color map) and Poynting vectors (black arrows) at absorption peaks (e-g) $p_a$ and (h-j) $p_b$ as indicated in (c), in (e-f, h-i) longitudinal planes cut by white dashed lines in (g, j) transverse planes, and vice versa. The green contours outline the $TiO_2$-electrolyte interface. (k) $A_{avg}$ (filled colors) and $\beta$ (blue lines) for wdp-MR configuration of $n_L = 4, 6, \cdots, 14$ log layers.

Unless otherwise specified, we consider a simple cubic wdp PC with $n_L = 4$ layers of identical $TiO_2$ woodpile logs (2 unit cells). As shown in Fig. 1(a), each log has a cuboid shape with equal width and height and infinite length, corresponding to a filling fraction (the fraction of total volume of the catalyst material) of 50%.

Optics EXPRESS

### 3.1. Optimized slow-light modes in simple cubic wdp PC for light trapping

The optimized slow-light modes for light trapping in the simple cubic wdp are investigated using the dispersionless dielectric Model I.01 for lightly doped anatase [43]. In Fig. 1(b) we plot the average absorptivity and its enhancement in the spectral region of $\lambda \in [400, 550]$ nm by varying the lattice constant $a$. Clearly, the enhancement factor $\beta$ exhibits a significant peak for $a \sim 240$ to 300 nm. The general tendency of rising $A_{\text{avg}}$ with increasing $a$ is due to the increase of overall $TiO_2$ volume.

To understand the dependence of $A_{\text{avg}}$ and $\beta$ on the lattice constant $a$, we plot the absorptivity and reflectivity of the 4-layer wdp-FS architecture in Fig. 1(c), depicted on top of the band diagram of wdp PC. When $a = 272$ nm, the absorption spectrum in the sub-gap spectral region of $\lambda \in [400, 550]$ nm ($a/\lambda \in [0.495, 0.680]$) features four strong absorption spikes between photonic bands 8 and 20. The average absorptivity $A_{\text{avg}}$ reaches 0.081, with an enhancement factor $\beta = 5.08$. When the lattice constant is increased to $a = 375$ nm, the same spectral region (now $a/\lambda \in [0.682, 0.938]$) shifts out of the scope of photonic bands 8 to 20 and enters into the region of bands 20 to 45. The associated photonic modes of the latter band region are not as absorptive or as efficiently excited, resulting in a dip in $\beta$ at $a = 375$ nm for the wdp-FS configuration in Fig. 1(b). When the lattice constant is further increased to $a = 600$ nm, higher order photonic modes between band numbers 70 and 190 shift down into the region of $\lambda \in [400, 550]$ nm, improving the absorptivity enhancement factor to $\beta = 4.12$ (with $A_{\text{avg}} = 0.147$).

To explore the mechanism of the strong light absorption in between photonic bands 8 to 20, we investigate the energy and Poynting vector distributions of absorption peaks marked in Fig. 1(c), $p_a$ at $a/\lambda = 0.574$ and $p_b$ at $a/\lambda = 0.625$. Here, we neglect the small imaginary part of the dielectric constant while keeping $\varepsilon' = 5.06$. Figures 1(e-j) show that in both cases the electromagnetic energy is concentrated in $TiO_2$ wdp backbone rather than in aqueous solution, as required for light harvesting in the photocatalyst. Moreover, from the patterns of the Poynting vector distribution, the energy flows primarily in the transverse plane of the wdp structure, perpendicular to the light incident direction. This is the parallel-to-interface-refraction (PIR) of normal incident light, which substantially increases the optical path length and light-matter interaction time for charge carrier photogeneration [43,62–66]. Due to these PIR slow-light modes, photonic bands 8 to 20 are remarkably effective for light trapping. The light absorptivity at $a/\lambda = 0.574$ reaches 0.711 in the dispersionless dielectric Model I.01.

When the transparent fused silica glass bottom support is replaced by a perfect mirror substrate, the average absorptivity is increased to $A_{\text{avg}} = 0.128$ and its enhancement factor reaches $\beta = 8.05$ for $\lambda \in [400, 550]$ nm at $a = 272$ nm, comparing with $\beta = 5.08$ for the wdp-FS architecture. The absorptivity enhancement is further increased to $\beta = 8.67$ (with $A_{\text{avg}} = 0.155$) at $a = 301$ nm, the optimized lattice constant for the wdp-MR configuration [see Fig. 1(d) for the absorption spectrum]. The perfect mirror substrate eliminates the transmission loss and in general increases the absorptivity by $\sim 2$ times [62,66], as depicted in Fig. 1(b). Similar to the invop PC, a reflective substrate shifts the optimum lattice constant of the wdp structure to larger values by about 10 to 50 nm [49]. In addition, the enhancement factor in the wdp-MR configuration exhibits a second maximum at $a \sim 627$ nm, with $A_{\text{avg}} = 0.281$ and $\beta = 7.53$. In such a case, the photonic band numbers in the region of $\lambda \in [400, 550]$ nm range from 80 to 210.

Experimentally, photonic modes between the 8th and 20th bands have been observed to demonstrate strong absorptivity enhancement in wdp structure with lattice constant 450 nm [43]. The observation of the high-lying photonic modes among the 80th and 210th, on the other hand, requires very high resolution fabrication. A larger lattice constant of $a \sim 627$ nm partially eases the fabrication challenge, but has yet to be demonstrated experimentally.

Increasing the number of woodpile logs $n_L$ raises the average absorptivity due to the increase of the active $TiO_2$ volume. However, the enhancement factor does not grow monotonically with $n_L$ due to the existence of optimized PC modes for light trapping and absorption saturation. In

Optics EXPRESS

Fig. 1(k) we investigate the wdp-MR configuration with $n_L$ = 4, 6, 8, 10, 12 and 14 woodpile log layers. At $a \sim 300$ nm, the average absorptivities dramatically increase for 6-, 10- and 14-layer wdp-MRs, while for 8- and 12-layer wdp-MRs the improvements are small. As a result the 8- and 12-layer wdp-MRs exhibit low $\beta$ around the optimized lattice constant $\sim$ 300 nm, while the 6-layer wdp-MR demonstrates the highest $\beta$. Similarly, for the wdp-FS architecture with optimized lattice constant $a \sim 270$ nm, $\beta$ = 4.9 for $n_L$ = 4 and 6, $\beta$ = 4.4 for $n_L$ = 10 and 14, $\beta$ = 4.0 for $n_L$ = 8 and $\beta$ = 3.8 for $n_L$ = 12. Therefore, the 6-layer wdp PC appears to be the most advantageous for light-trapping. We focus on the 4-layer wdp PC in this work due to its facile fabrication. In the next subsection we align the photonic modes between the 8th and 20th bands with the sub-gap region of $TiO_2$ in a 4-layer wdp PC, taking into account the material dispersion at and above the electronic band gap.

### 3.2. *Light harvesting by wdp PC in the UV-visible spectral range*

We now discuss the optimized lattice constant of wdp structure placed on a MR substrate using the dispersive dielectric Model II in the spectral region from 282 nm to 550 nm. The MAPD and its enhancement factor $\zeta$ are the criteria we use to evaluate wdp structures in this subsection.

From Fig. 2(a), the optimum lattice constant for light harvesting using wdp-MR configuration is $a \sim 350$ nm. We break the MAPD of the entire UV-visible spectral range into contributions from the UV ($\lambda \in [282, 400]$ nm) and the visible ($\lambda \in [400, 550]$ nm) regions. In the UV region, the MAPD and its enhancement $\zeta$ remain flat as functions of $a$, due to the large intrinsic absorptivity and the scarcity of sunlight. In the visible region, the MAPD enhancement exhibits a

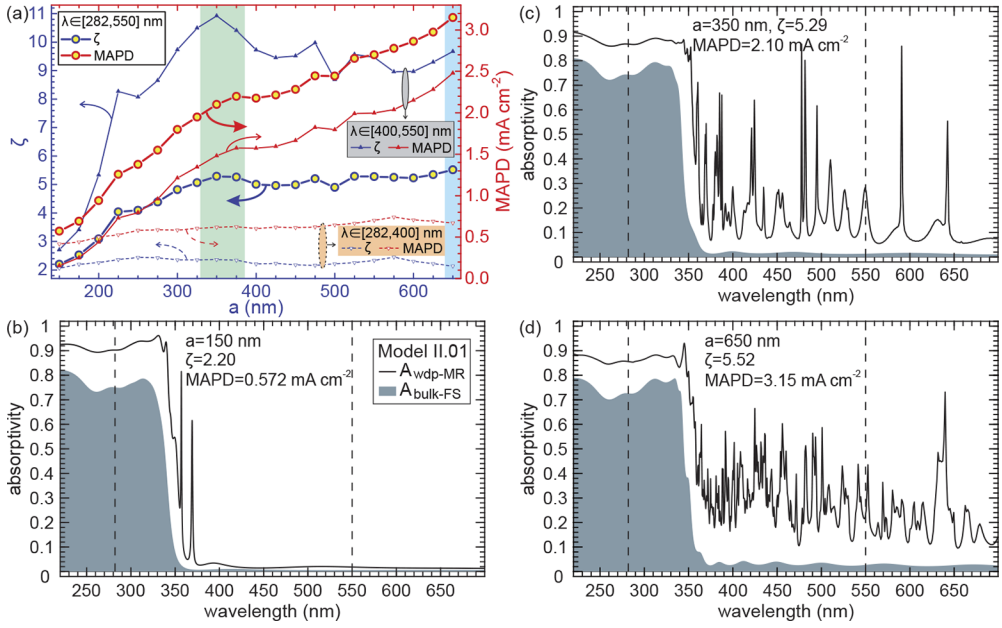


**Fig. 2.** Light harvesting of 4-layer $TiO_2$ simple cubic woodpile PC on MR substrate using the dispersive dielectric Model II.01. (a) The MAPD (red lines) and its enhancement factor $\zeta$ (blue lines) in different wavelength regions, with color shades highlighting the optimized ranges of the lattice constant $a$. (b-d) Absorptivity spectra (black lines) of wdp-MR architectures and planar $TiO_2$ films with equivalent bulk thicknesses on FS substrates (gray-blue filled color). The vertical black dashed lines demark $\lambda \in [282, 550]$ nm regions for (b) $a$ = 150 nm, (c) $a$ = 350 nm, and (d) $a$ = 650 nm, respectively, for which $\zeta$ and MAPD are calculated.

Optics EXPRESS

peak at $a = 350$ nm due to the strong light trapping ability of the photonic modes between bands 8 to 20. Since the photon numbers in the $\lambda \in [400, 550]$ nm are six times that in the UV range, the optimum lattice constant for the entire UV-visible range is determined by the visible light harvesting. The enhancement in 4-layer wdp-MR configuration as a function of lattice constant is more flat [Fig. 2(a)] than for the invop PC [49]. This reduced sensitivity to variation in lattice constant suggests that fabrication requirements are likewise less stringent.

The absorption spectra of wdp-MR configuration for different lattice constants are given in Figs. 2(b-d). At $a = 150$ nm, low order photonic modes fall into the vicinity of the $TiO_2$ electronic band edge, giving rise to an MAPD enhancement factor of $\zeta = 2.20$. This enhancement is weak as it comes solely from the UV region with scarce sunlight. As the lattice constant increases, higher order photonic modes shift to the UV-visible frequency range. At $a = 350$ nm, optimum photonic bands 8 to 20 emerge in the visible light region, dramatically increasing $\zeta$ to 5.29. At $a = 650$ nm, much higher order photonic bands are activated in the $\lambda \in [282, 550]$ nm range, leading to an MAPD enhancement factor of $\zeta = 5.52$. As more photonic bands (of higher orders) are placed in this spectral region (using larger lattice constant), the absorption enhancement is much more broadband than for the case of $a = 150$ nm.

The delicate and precise layer-by-layer fabrication of the wdp PC enables the use of high order photonic bands. As a result, large absorptivity and MAPD enhancements can be achieved with small PC thickness because normal incident light is diffracted into high order slow-light modes, propagating laterally in the PC film, ensuring longer light-matter interaction time. Small PC thickness then enables efficient charge carrier collection. However, the large-scale fabrication of high quality woodpiles may be expensive, making this architecture challenging for broad application.

## 4. Square lattice nanorod PC

Nanorods and/or nanowires are widely studied in photovoltaics and photocatalysis. In photoelectrochemical cells [67], they have shown enhancement in carrier photogeneration and good charge carrier transport in the catalyst. The advantage of nanorods, comparing with planar photoelectrodes, lies in the dissociation of light absorption and minority charge carrier collection. A long nanorod length may enhance absorptivity of light propagating along the rod axis, while a small nanorod diameter may reduce the distance that minority charges need to diffuse to the catalyst surface before bulk recombination. Moreover, nanorods provide a large surface area for chemical redox reactions at the semiconductor-electrolyte interface.

We consider nanorod PC (nrPC) in the form of a 2D square lattice of identical nanorods with lattice constant $a$, rod radius $r$ and length $h$ [see Fig. 3(a)]. Here, light trapping is enhanced by a densely distributed set of photonic Bloch modes, compared to the sparse leaky modes for individual, isolated nanorods [65,68,69]. The optical absorption of square lattice nrPCs has been theoretically investigated for materials of Si [70–74], InP [73,75], and GaAs [73,74,76]. Highly ordered nanorod arrays have been fabricated using various dry etching and chemical deposition methods [77] with Si [78–80], Ge [81], GaN [82], InAs [83], InP [84], ZnO [85], etc., demonstrating enhanced light trapping [79,80].

However, previous studies of $TiO_2$ nanorod solar cells [86] and photocalysis [87] have focused on non-periodic arrays synthesized by bottom-up approaches such as hydrothermal [86,87], metal-organic chemical vapor deposition (MOCVD) [88] and sol-gel [89] methods. A few ordered $TiO_2$ nanorod arrays were fabricated using pulsed laser deposition [90], oblique angle deposition [91] and photoelectrochemical etching [92] with limited control over the geometric shape. High qualitity $TiO_2$ nrPC with wide range tunability of the PC lattice constants, rod radii and rod lengths may be potentially fabricated by techniques such as MOCVD.

Optics EXPRESS

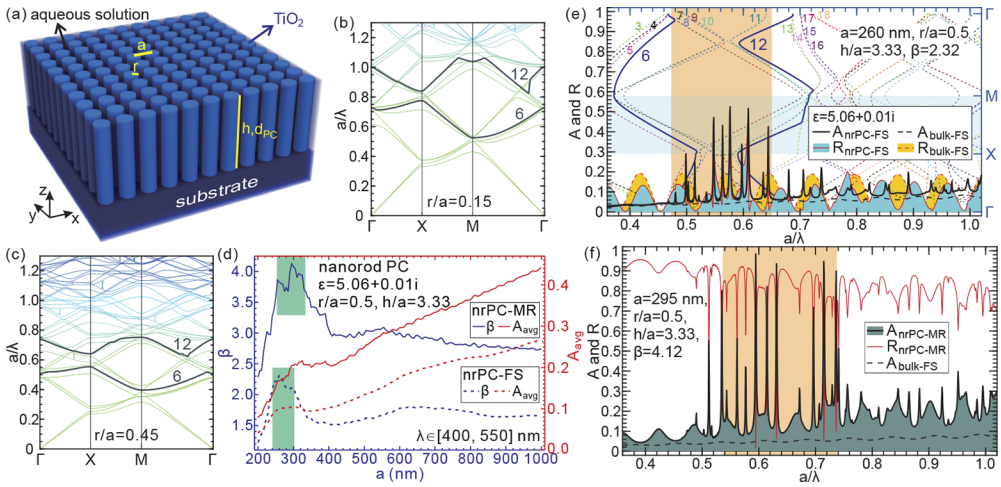


**Fig. 3.** Light trapping of $TiO_2$ square lattice nanorod PC in aqueous solution for $\lambda \in [400, 550]$ nm using the dispersionless dielectric Model I.01. (a) Illustration of nrPC with lattice constant $a$, rod radius $r$ and rod length $h$. (b, c) The band diagrams of nrPC in aqueous solution of $r/a = 0.15$ and 0.45, respectively, with the 6th and 12th photonic bands highlighted. (d) $A_{\text{avg}}$ (red lines) and $\beta$ (blue lines) for nrPC-FS (dashed lines) and nrPC-MR (solid lines) architectures, with color shades highlighting the optimized ranges of $a$. (e, f) Spectra of absorptivity $A$ and reflectivity $R$ of (e) nrPC-FS and (f) nrPC-MR with $r/a = 0.5$ and $h/a = 3.33$, and bulk-FS architectures. The background color lines depict the band diagram of the corresponding nrPC in aqueous solution, with band numbers 3 to 18 labeled on top. The orange shadings demark $\lambda \in [400, 550]$ nm regions for (e) $a = 260$ nm and (f) $a = 295$ nm.

### 4.1. *Optimized slow-light modes in nrPC for light trapping*

We first investigate light trapping of nrPCs in the sub-gap region of $TiO_2$ to identify the optimum lattice constant and photonic band region for visible light harvesting using the dispersionless dielectric Model I.01. In Figs. 3(b, c) we plot the 2D band diagrams of nrPC in aqueous solution for $r/a = 0.15$ and 0.45. Photonic bands shift towards lower frequency as the lattice constant $a$ increases (both for fixed $r/a$ ratio and fixed $r$ alone). Increasing $r$, for fixed $a$, also pulls higher order bands down in frequency. The aim is to place a high spectral density of slow-light modes into the 400 - 550 nm band. Both light trapping and absorption are enhanced by a large $r/a$ ratio. In this subsection, we focus on the close-packed limit of $r/a = 0.5$, corresponding to a filling fraction of $F = 78.54\%$. The variation of $r/a$ is further discussed in Sec. 4.2.

In Fig. 3(d) we plot the average absorptivity and its enhancement $\beta$ for both nrPC-FS and nrPC-MR architectures with nanorod length $h = 3.33a$ using dielectric Model I.01 for $\lambda \in [400, 550]$ nm. The optimized lattice constant is around $\sim 300$ nm. At $a = 260$ nm, the nrPC-FS architecture demonstrates $A_{\text{avg}} = 0.102$ and $\beta = 2.32$, while at $a = 295$ nm the nrPC-MR architecture demonstrates $A_{\text{avg}} = 0.204$ and $\beta = 4.12$. The corresponding spectra of absorptivity $A$ and reflectivity $R$ are illustrated in Fig. 3(e) for nrPC-FS and 3(f) for nrPC-MR architectures.

From Fig. 3(e), both the nrPC and planar $TiO_2$ film demonstrate regular multiple reflection peaks due to interference. The nrPC generally reduces the reflectivity compared with the planar thin film structure [69,84,93,94]. The contrast, however, is small in Fig. 3(e) due to the high filling fraction in our example. Nevertheless, the 2D nrPC demonstrates smaller reflectivity comparing with the three-dimensional (3D) PCs such as invop [see Figs. 10(c-e)] and wdp [see Fig. 1(c)] structures. This makes nrPC a good anti-reflection [70,76] layer in composite architectures of photocatalyst.

Optics EXPRESS

The absorption spectra in Figs. 3(e, f) exhibit a series of strong resonant peaks. These highly absorptive resonances, marked by orange shadings, are photonic modes between band numbers 6 and 12. They are placed in the $TiO_2$ subgap of [400, 550] nm by proper choice of lattice constant $a$ = 260 nm for nrPC-FS and $a$ = 295 nm for nrPC-MR. Outside this region the PC photonic modes become less absorptive. For fixed $h/a$ and $r/a$, this results in a linear increase of $A_{avg}$ as a function of $a$ for $a$>400 nm in Fig. 3(d).

### 4.2. *Light harvesting by nrPC in the UV-visible spectral range*

The influences of the lattice constant, nanorod radii and lengths on optical absorption have been theoretically investigated for narrower bandgap semiconductors such as Si, Ge, InP, GaAs, InGaP, CdTe [70,71,73–76]. The $TiO_2$ nrPC has substantially different material dispersion and requires its own optimization (using dielectric Model II.01) for light harvesting in the 282 - 550 nm range and for comparison with other $TiO_2$ PC structures.

In Figs. 4(a, b), the MAPD and its enhancement $\zeta$ are plotted for nrPC-MR architecture for different geometries with nonorod length of $h$ = 1.3 $\mu$m. In Fig. 4(a) and the inset of Fig. 4(b) we vary $a$ by fixing $r$ = 80 nm and $r/a$ = 0.48474, respectively. The choice of $r/a$ in the inset of Fig. 4(b) corresponds to a filling fraction of $F$ = 73.82% that enables a direct comparison with the scPore structure with $r = 0.5a$ in Sec. 5.2 [see Figs. 6(a, b)]. From Fig. 4(a), both MAPD

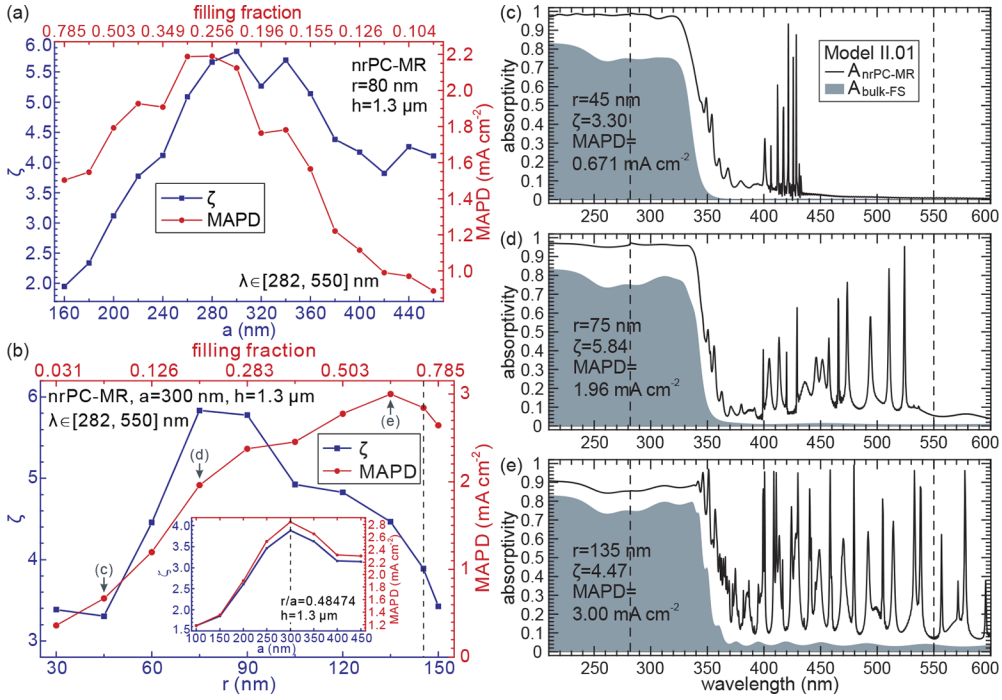


**Fig. 4.** Light harvesting of a $TiO_2$ square lattice nrPC-MR architecture for $\lambda \in [282, 550]$ nm using the dielectric Model II.01. (a, b) MAPD (red lines) and $\zeta$ (blue lines) for nrPC-MR with $h$ = 1.3 $\mu$m as functions of (a) $a$ for fixed $r$ = 80 nm and (b) $r$ for fixed $a$ = 300 nm. The inset in (b) shows that the optimum lattice constant is $a$ = 300 nm for fixed $h$ = 1.3 $\mu$m and $r/a$ = 0.48474 ($F$ = 73.82%, marked by the vertical dashed black line in the main plot). (c-e) Absorptivity spectra of nrPC-MR (black lines), with $a$ = 300 nm and $h$ = 1.3 $\mu$m, and bulk-FS (gray-blue filled color) architectures for (c) $r$ = 45 nm, (d) $r$ = 75 nm, and (e) $r$ = 135 nm. The vertical black dashed lines demark $\lambda \in [282, 550]$ nm regions for which $\zeta$ and MAPD are calculated.

Optics EXPRESS

and $\zeta$ increase as $a$ reduces from $\sim$ 420 nm. The optimum lattice constant, as shown in Figs. 4(a, b), is $\sim$ 300 nm. A lattice constant smaller than $\sim$ 260 nm reduces the light trapping strongly despite the increase of the filling fraction.

In the main plot of Fig. 4(b), we fix the lattice constant $a$ = 300 nm and nonorod length $h$ = 1.3 $\mu$m and vary the nanorod radius (and the filling fraction, accordingly). The MAPD increases with $r$ from $r$ = 30 nm (0.36 mA cm$^{-2}$) to $r$ = 135 nm (3.00 mA cm$^{-2}$), due to the emergence of light-trapping PC modes and the increase in volume of absorptive $TiO_2$. Further increase of $r$ strongly suppresses light trapping in nrPC, reducing the MAPD in spite of the increase in absorptive material volume. Light trapping optimization is seen from the MAPD enhancement factor $\zeta$, which exhibits a peak in the $r$ = 75 to 90 nm range (i.e., $r/a \in [0.25, 0.3]$). The enhancement factor $\zeta$ reaches 5.84 (where MAPD = 1.96 mA cm$^{-2}$) at $r$ = 75 nm for $\lambda \in [282, 550]$ nm.

To explain the dependence of MAPD and $\zeta$ on $r$, we plot the absorption spectra of nrPC-MR with $a$ = 300 nm, $h$ = 1.3 $\mu$m for three different nanorod radii $r$ = 45, 75, and 135 nm in Figs. 4(c-e). For the sparse nrPC with $r/a$ = 0.15, the strongly absorptive photonic modes are confined to the spectral region of $\lambda \in [400, 430]$ nm. As the $r/a$ increases to 0.25, these modes move to the spectral region of interest from 400 to 550 nm. This dramatically increases $\zeta$ as shown in Fig. 4(b). This trend agrees with the band diagrams in Figs. 3(b, c), showing red shifts with increasing rod radius $r$. The PC light trapping saturates when the nanorod radius increases to 135 nm with $r/a$ = 0.45. This provides the best MAPD of 3.0 mA cm$^{-2}$, but reduces the MAPD enhancement factor $\zeta$. The maximum enhancement occurs when the nrPC has a filling fraction $F \sim$ 20% - 30%, whereas the best MAPD is realized near close-packing. In the next section we discuss a better 2D structure that further suppresses the reflection of incident light by a gradient refractive index.

## 5. Square lattice slanted conical-pore PC

We now consider a square lattice of conical pores etched into bulk $TiO_2$. In the slanted version of this structure, namely, slanted conical-pore (scPore), each pore has an oblique orientation, with the apex aligned away from below the base center [see Figs. 5(a) and 11]. The scPore PC exhibits strong synergy between the photonic slow-light modes and reduced reflection loss due to its graded refractive index profile [58,95–97]. Recently, scPore PC was suggested as a photoelectrode for solar fuel generation in photoelectrochemical cell, demonstrating superior light trapping and charge transport comparing with traditional structures of photoelectrode [58]. Similar PCs of inverted pyramids with periodicity 500 nm to 1500 nm [98,99] and parabolic-pores of lattice constant 1.2 $\mu$m [100] have been fabricated on crystalline silicon using wet and dry etching methods, respectively. Both have comparable light trapping abilities [101].

As shown in Figs. 5(a) and 11, the scPore PC is characterized by four parameters: the square lattice constant $a$, the raidus $r$ of the base of the cone, the height $h$ of the cone, and the slant distance $p$. In this work, unless otherwise specified, we assume $p = r$ [meaning the apex of the cone is vertically aligned to the edge of the base of the cone as in Fig. 5(a)] and mainly discuss $a = 2r$ (filling fraction $F$ = 73.82%) and $a = 1.739r$ ($F$ = 66.09%, see Appendix C for details).

### 5.1. Light trapping by scPore PC in the sub-gap region of $TiO_2$

We first investigate the influence of the slant distance $p$ on light trapping in scPore PCs using the dispersionless dielectric Model I.01. In Fig. 5(b) we consider an scPore PC on fused silica glass substrate with $r = 0.5a$ and $h = 3.71a$. The absorptivity enhancement is significant around $a$ = 300 nm, as well as $a \sim$ 850 nm for $p/r$ in the range of 0.4 to 0.9. The smaller lattice constant utilizes lower order resonant photonic modes, which are more robust against lattice disorder. Moreover, it reduces the necessary distance that photogenerated minority charge carriers have to diffuse to reach the reaction sites on the $TiO_2$-electrolyte interface. For $a \sim$ 300 nm, the

Optics EXPRESS

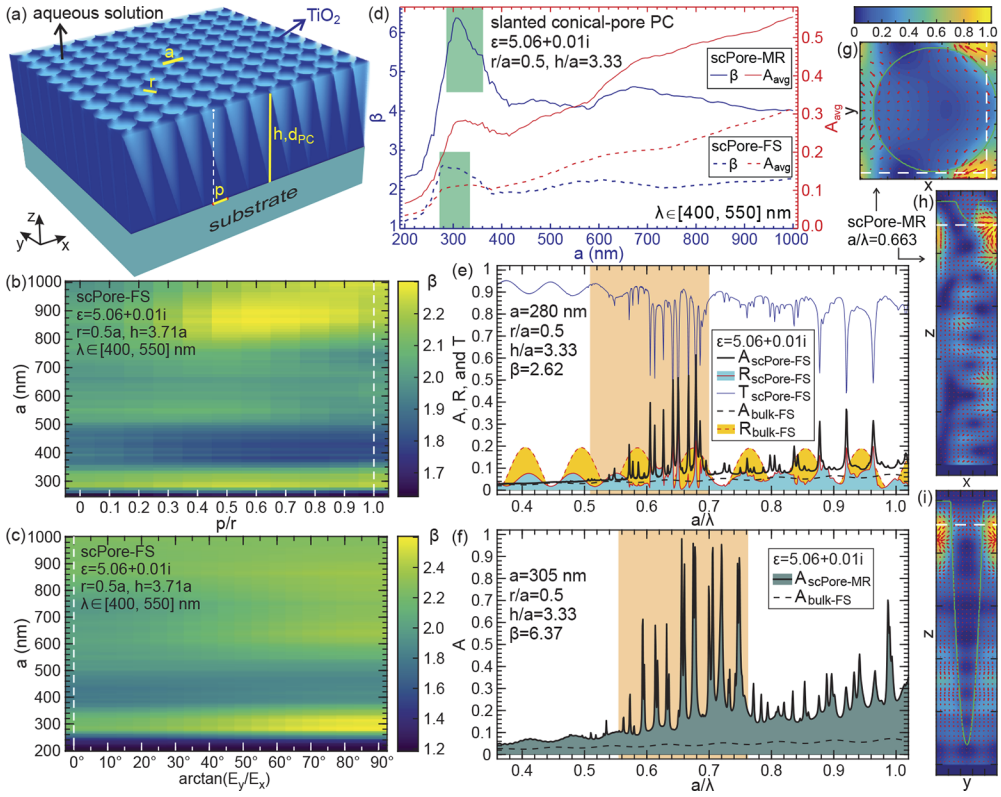


**Fig. 5.** Light trapping of $TiO_2$ square lattice (slanted) conical-pore in aqueous solution for $\lambda \in [400, 550]$ nm using the dispersionless dielectric Model I.01. (a) Illustration of scPore with lattice constant $a$, base radius $r$, cone height $h$, and the slant distance $p = r$. (b) Color map of $\beta$ for scPore-FS architecture as a function of $a$ and $p/r$ (slanted to the positive $x$-direction) under normal, $x$-polarized incidence. (c) $\beta$ for scPore-FS with $r = 0.5a$, $h = 3.71a$ and $p = r$, as a function of $a$ and the polarization angle of incident light. (d) $A_{\text{avg}}$ (red lines) and $\beta$ (blue lines) for scPore-FS (dashed lines) and scPore-MR (solid lines) of $r = 0.5a$ and $h = 3.33a$, with color shades highlighting the optimized ranges of $a$. (e, f) The spectra of $A$, $R$ and transmissivity $T$ of (e) scPore-FS, (f) scPore-MR, and bulk-FS architectures. The vertical orange shadings demark $\lambda \in [400, 550]$ nm region for (e) $a = 280$ nm and (f) $a = 305$ nm, respectively, for which $\beta$ is calculated. (g-i) Distributions of electromagnetic energies (color map) and Poynting vectors (red arrows) at $a/\lambda = 0.663$ of an scPore-MR architecture along (g) transverse and (h, i) longitudinal planes indicated by the white dashed lines in (h, i) and (g), respectively. The solid green lines depict the $TiO_2$-electrolyte interface.

Optics EXPRESS

conical-pore PC with oblique cones ($p/r \neq 0$) demonstrates stronger absorption enhancement than right cones ($p/r = 0$). In what follows we consider $p/r = 1$, with the apex of the cone shifted to the positive $x$-direction [see Fig. 5(a)].

Since the scPore PC is anisotropic, it is worthwhile to consider the response to different polarizations of incident light. In Fig. 5(c) we change the polarization angle of the normal incident light with respect to the slant direction ($x$) of the scPore PC on FS substrate. The polarization angle is defined as $\arctan(E_y/E_x)$, where $E_{x,y}$ are the $x$- and $y$-components of the electric field of the incident irradiation. Figure 5(c) shows the absorptivity increases with the polarization angle. Namely, a $y$-polarized photon is absorbed more strongly than an $x$-polarized photon by an scPore PC slanted to the $x$-direction. This is true for both scPore-FS and scPore-MR architectures. In this paper (unless otherwise specified), we consider $x$-polarized incident light. The absorption of unpolarized solar light by the scPore PC is, therefore, stronger than our depictions for $x$-polarized light.

In Fig. 5(d) we plot the average absorptivity $A_{\text{avg}}$ and its enhancement factor $\beta$ by varying the lattice constant $a$ for fixed $r = 0.5a$ and $h = 3.33a$. It is seen that for both scPore-FS and scPore-MR architectures, $a \sim 300$ nm is the optimum lattice constant for light trapping. This is independent of the height of the PC. At $a = 280$ nm, the scPore-FS architecture demonstrates $A_{\text{avg}} = 0.105$ and $\beta = 2.62$, while at $a = 305$ nm, the scPore-MR architecture demonstrates $A_{\text{avg}} = 0.279$ and $\beta = 6.37$.

The corresponding spectra of absorptivity $A$, reflectivity $R$, and transmissivity $T$ of the scPore PC are illustrated in Figs. 5(e, f). The reflectivity of scPore-FS is noticeably smaller than that of a planar film on fused silica glass. The filling fraction of the scPore PC ($F = 73.82\%$) shown in Fig. 5(e) is similar to that of the nrPC ($F = 78.54\%$) shown in Fig. 3(e), and the ratio $h/a = 3.33$ is the same. This enables a direct comparison of the anti-reflection properties of these two types of PCs. Clearly, the scPore PC exhibits better anti-reflection effect than the nrPC. The latter, nevertheless, is less reflective than the invop and wdp PCs.

When $a = 280$ nm, dense group of absorption spikes appears in the $\lambda \in [400, 550]$ nm region [see Fig. 5(e)], corresponding to optimized light trapping. Unlike invop and wdp structures, the reflectivity of scPore on fused silica glass substrate remains small in the entire spectral region from $a/\lambda = 0.4$ to 1.8. Instead, the transmissivity can be used experimentally to identify the optimized light-trapping parameters for the scPore-FS architecture. When the scPore PC is placed on a perfect mirror substrate, a higher density of stronger absorption peaks appears in $\lambda \in [400, 550]$ nm range at $a = 305$ nm as shown in Fig. 5(f). This leads to $\beta = 6.37$, in contrast to $\beta = 2.62$ for the scPore-FS architecture at $a = 280$ nm.

A close inspection of highly absorptive photonic modes reveals PIR slow light in the optimized scPore structure. Figures 5(g-i) illustrate the electromagnetic energy and Poynting vector distributions at the frequency of $a/\lambda = 0.663$ ($\lambda = 452$ nm for $a = 300$ nm), assuming $\varepsilon = 5.06$ for $TiO_2$. Significant energy flux flows transversely around the conical pore, enabling high absorptivity of normal incident light with small thickness of the PC.

### 5.2. Light harvesting by scPore PC in the UV-visible spectral range

In this subsection we optimize sunlight harvesting of the scPore-MR architecture in the UV to visible spectrum using the dispersive dielectric Model II.01, taking into account the realistic $TiO_2$ material dispersion. In Fig. 6(a), we vary the lattice constant $a$ with fixed $r/a = 0.5$ and cone height $h = 1.3$ $\mu$m. In contrast to the result for the visible spectrum in Sec. 5.1, the optimum $a$ now shifts from $\sim 300$ nm to 350 nm as a result of material dispersion, above-gap absorption and the actual solar spectrum. With the same filling fraction $F = 73.82\%$ and PC thickness 1.3 $\mu$m, scPore-MR demonstrates superior light trapping compared with nrPC-MR architecture [see Fig. 4(b)].

Optics EXPRESS

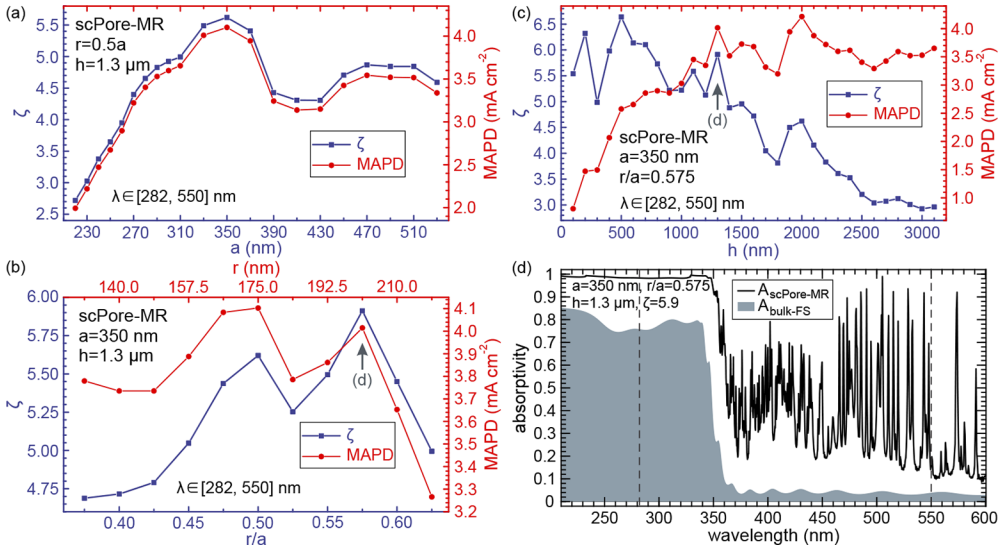


**Fig. 6.** Light trapping of square lattice scPore-MR in aqueous solution for $\lambda \in [282, 550]$ nm using the dispersive dielectric Model II.01. (a-c) The MAPD and $\zeta$ as functions of the lattice constant $a$, base radius $r$, and pore depth $h$. (d) Absorptivity spectrum of scPore-MR (black line), with $a = 350$ nm, $r = 0.575a$ and $h = 1.3$ $\mu$m [corresponding to dark green arrows in (b) and (c)], and bulk-FS (gray-blue filled color) architectures. The vertical black dashed lines demark $\lambda \in [282, 550]$ nm region in which $\zeta$ and MAPD are calculated.

In Fig. 6(b) we optimize $r$ by fixing the optimum $a = 350$ nm and assuming $h = 1.3$ $\mu$m. Two optimum radii of the cone base become apparent: $r = 0.5a$ and $r = 0.575a$. We note that the filling fraction decreases as $r/a$ increases (see Appendix C for details). Stronger MAPD enhancement can occur with less $TiO_2$. Specifically, $\zeta$ is 5.62 for $r = 0.5a$, whereas it reaches 5.91 for $r = 0.575a$.

Lastly, we investigate the influence of the cone height $h$ by fixing the optimized $a = 350$ nm and $r = 0.575a$. Increasing $h$ increases the $TiO_2$ volume with fixed filling fraction. This raises the MAPD and decreases its enhancement (due to absorption saturation), as seen in Fig. 6(c). Of particular interest is the rate of increase of MAPD with cone height. Figure 6(c) reveals two distinct regimes of MAPD: $h \lesssim 1100$ nm and $h \gtrsim 1100$ nm. The former regime exhibits rapid increase of MAPD with $h$ and remarkable PC light trapping. When $h = 500$ nm, $\zeta$ reaches 6.64 (with MAPD = 2.58 mA cm$^{-2}$). For $h$>1100 nm, the increase of the light absorptivity becomes slower and $\zeta$ drops. When $h = 2.0$ $\mu$m, MAPD reaches 4.21 mA cm$^{-2}$ with $\zeta = 4.62$.

Figure 6(d) shows the absorptivity spectrum of an scPore PC, on perfect mirror substrate, with $a = 350$ nm, $r = 201.3$ nm and $h = 1.3$ $\mu$m. This structure exhibits MAPD of 4 mA cm$^{-2}$ and enhancement factor of $\zeta = 5.91$. The visible light absorptivity is strongly enhanced, and the UV light absorptivity is increased to near unity.

## 6. Comparison of light trapping in optimized photonic crystals

We now compare the simple cubic woodpile, slanted conical-pore, and nanorod PC with each other and the more widely studied inverse opal PC. The optimization of the invop PC is described in Ref. [49]. Structural and light trapping properties of the invop PC are provided in Appendix B.

We first compare the average absorptivities for different PC-MR architectures in the sub-gap region $\lambda \in [400, 550]$ nm of pristine $TiO_2$ described by the dispersionless dielectric Model I.001 (i.e., $\varepsilon = 5.06 + 0.001i$). The comparison is made with respect to the equivalent bulk thickness

Optics EXPRESS

$d_{TiO_2}$ and the overall PC thickness $d_{PC}$. For a given volume filling fraction $F$, $d_{TiO_2}$ and $d_{PC}$ can be varied by rescaling the whole PC (keeping the fixed ratios of the structural parameters). Alternatively, the number of layers $n_L$ (for invop and wdp PCs) or the height $h$ of the elementary structure (for scPore and nrPC) can be changed. Experimentally, the wdp PC favors overall rescaling since it is difficult to align a large number of layers of woodpile logs using layer-by-layer fabrication. On the other hand, the overall thickness of the invop PC is easily increased by deposition and self-assembly of opal spheres [102]. Here we focus on the second way as it preserves the optimum photonic bands in frequency for comparison.

The light absorptivities as a function of $d_{TiO_2}$ illustrate the light trapping capabilities of the PC structures. In Fig. 7(a), we fix the lattice constant for each type of PC to its optimum and vary $d_{TiO_2}$. The optimized invop-MR architecture has $D \sim 350$ nm [49], and the optimized wdp-MR, nrPC-MR and scPore-MR architectures have $a \sim 300$ nm. Comparing the four optimized structures the rank of light trapping capability for given mass of $TiO_2$ (fixed $d_{TiO_2}$) is invop-MR > scPore-MR > wdp-MR > nrPC-MR.

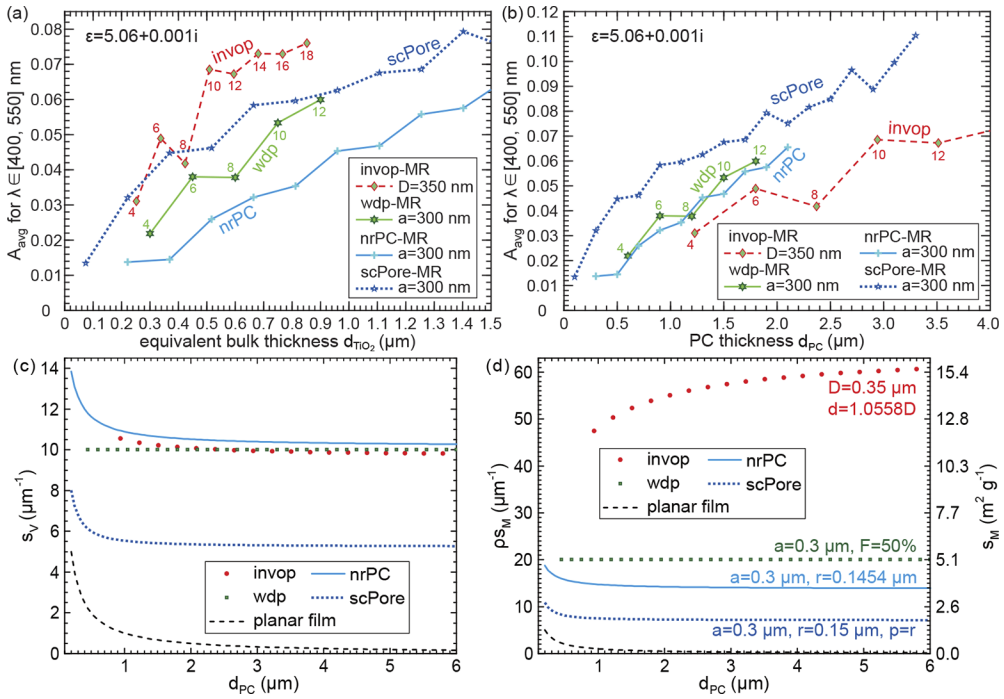


**Fig. 7.** Comparisons of the (a, b) average absorptivities $A_{avg}$ for $\lambda \in [400, 550]$ nm, (c) volume-specific surface area $s_V$, and (d) mass-specific surface area $s_M$ of the face-centered cubic inverse opal, simple cubic woodpile, square lattice nanorod, and square lattice slanted conical-pore PCs on highly reflective perfect mirror substrates. Comparisons are made with respect to (a) $d_{TiO_2}$ and (b-d) $d_{PC}$, using the dispersionless dielectric Model I.001 with $\varepsilon = 5.06 + 0.001i$. $d_{TiO_2}$ and $d_{PC}$ are varied by changing the number of layers $n_L$, or cone and/or nanorod heights, with fixed lattice constant $a$. The numbers 4, 6, $\cdots$, 18 in (a, b) indicate the number of woodpile log layers for wdp PC and opal layers for invop PC. The mass density of $TiO_2$ is assumed to be $\rho = 3.9$ g cm$^{-3}$ in (d). The structural parameters are fixed as follows: For invop, $d = 1.0558D$ (where $d$ is the diameter of the opal sphere and $D$ is the center-to-center distance between adjacent spheres). For wdp, the height and width of each woodpile log are $a/2$. For nrPC, $r = 0.48474a$ and for scPore, $r = a/2$ and $p = r$. The nrPC and scPore PC have the same filling fraction $F = 73.82\%$.

Optics EXPRESS

A comparison based on $d_{PC}$ involves both the PC light trapping for photogeneration and the subsequent charge carriers transport. In Fig. 7(b), the absorptivities of the same structures as in Fig. 7(a) are plotted as functions of $d_{PC}$ instead of $d_{TiO_2}$. Clearly, the ranking of the light trapping capability for fixed PC height becomes scPore-MR > wdp-MR ~ nrPC-MR > invop-MR. This is due in part to their relative volume filling fractions: $F_{scPore} = 73.82\%$, $F_{wdp} = 50\%$, and $F_{invop,n_L=\infty} = 15\%$ (see Appendix B.1 for the $n_L$-dependent filling fraction of inovp PC).

In applications such as photoelectrochemical cell for water splitting, photogenerated electrons are collected by the bottom contact (photocathode) for reduction reactions, while holes move to the semiconductor-electrolyte interface (photoanode) for oxidation reactions. Charge separation and transport are heavily influenced by the structure of the photocatalyst [58]. Typically, in a n-type semiconductor, the minority carriers (holes) have much shorter diffusion length than the majority carriers (electrons). The photocatalyst structure should (i) trap light strongly, (ii) possess hierarchical length scales appropriate to the electron and hole diffusions, and (iii) provide straight conduction path for charge collection.

In PC structures the emergence of the PIR slow-light modes steers the normal incident light into the effectively infinite transverse plane of the photocatalyst. It significantly enhances the light absorptivity and decouples the photon propagation and the primary longitudinal charge conduction pathways. This alleviates the strong mismatch between the long light absorption length and the short charge diffusion length, therefore reduces the necessary catalyst thickness for photogeneration and, in turn, decreases the charge recombination during diffusion. In our PC architectures the relevant hierarchical length scales are the lattice constant, $a$, and the PC thickness, $d_{PC}$. In general, photogenerated holes need only to diffuse $\lesssim a/2$ to reach the reaction sites on the surface of the catalyst, while the photogenerated electrons have to diffuse $\gtrsim d_{PC}$ to be collected by the substrate. In $TiO_2$, the hole diffusion length is ~ 10 - 300 nm [103–106] and the electron diffusion length is ~ 10 $\mu$m [59]. The former length scale roughly matches the optimum lattice constants $a \sim 300$ nm of wdp, nrPC and scPore structures. For invop structure, the necessary distance holes travel to the catalyst surface is determined by the thin scaffold wall which is typically much smaller than $a/2$. However, electrons must traverse a very precarious path to reach a bottom contact.

Both the scPore PC and nrPC offer straight conduction paths for majority charge carriers (electrons for n-type $TiO_2$) to the bottom contacts. Their similar morphology suggests they have comparable charge carrier transport properties. For comparison we choose their filling fractions to be the same in Fig. 7. The scPore-MR is clearly superior to nrPC-MR in light trapping capability. There are also some straight conduction paths for electrons in the wdp structure, but the interfaces of different woodpile logs may contain a high density of recombination centers. The invop structure does not provide any straight electron conduction paths [58], resulting in propitious charge carrier recombination.

Large specific surface area of the photocatalyst structure may boost reaction rates by increasing the exposure to the reactants. The volume-specific surface area of a PC is $s_V = S_{tot}/V_{PC}$, where $S_{tot}$ and $V_{PC}$ are the total surface area and volume, respectively, of a column of PC unit cells. For wdp PC with 50% filling fraction, $S_{tot} = (3/2)n_L a^2$, and for nrPC with $r \leqslant a/2$, $S_{tot} = \pi r^2 + 2\pi rh$. So $s_V = 3/a$ for wdp PC and $s_V = [\pi r(r + 2h)]/(a^2 h)$ for nrPC. The mass-specific surface area is $s_V/(\rho F)$, where $\rho$ is the mass density of $TiO_2$. The analytical expressions of volume- ($s_V$) and mass-specific ($s_M$) surface areas of invop and scPore PCs are given in Appendices B.1 and C, respectively. In Figs. 7(c, d) we compare specific surface areas of different PCs shown in Figs. 7(a, b) as functions of PC thickness.

From Figs. 7(c, d), the wdp, nrPC and invop structures have similarly large volume-specific area ~ 10 $\mu m^{-1}$. The invop PC exhibits the largest mass-specific surface area due to its porous structure. On the other hand, the scPore PC has noticeably less $s_V$ and $s_M$. However, additional surface area can be introduced by texturing the inner surfaces of the scPore PC with nanowires

Optics EXPRESS

[58], similar to ZnO nanowires integrated on top of $TiO_2$ invop PC [107] and $TiO_2$ nanowires grown on silicon rods [108]. Augmented surface area of this nature has been shown to enhance the photoelectrochemical activity [109].

## 7. Conclusion

The Achilles heel of titania-based photocatalysis is its low efficiency under sunlight due to poor visible-light absorptivity. Strong modification on $TiO_2$ by heavy-doping often introduces excess recombination centers deteriorating the charge transport. Using lightly doped $TiO_2$ as a weak absorber in the sub-gap region and shaping it into photonic crystal (PC) architecture, the electron-hole recombination can be minimized while the photogeneration can be significantly enhanced through resonant photonic slow-light modes. Specific PC structures not only enable strong wave-interference-based light trapping, but also branch electron and hole diffusions, further diminishing charge carrier recombination. Parallel-to-interface-refraction, photonic modes decouple the light absorption from the charge conduction by guiding the normal incident light into transverse directions, increasing light-matter interaction time without proliferating the electron diffusion path. Therefore, strong photogeneration is achieved with small PC thickness which, in turn, reduces carrier loss. We compared four optimized PC structures of lightly doped $TiO_2$ for sunlight harvesting in the UV (above-gap) to visible (sub-gap) spectral range $\lambda \in [282, 550]$ nm, which is summarized in Table 1. Similar results apply to other wide-band semiconductor photocatalysts.

**Table 1. Optimization of four PC structures on perfect mirror substrates for light harvesting in $\lambda \in [282, 550]$ nm range assuming dispersive dielectric Model II.01.**

| PC | Optimization | | | | | | Example | | |
|---|---|---|---|---|---|---|---|---|---|
| | $a$ (nm) | $r$ (nm) | $p$ | $F$ | $n_L$ | bands | $d_{PC}$ ($\mu$m) | MAPD (mA cm$^{-2}$) | $\zeta$ |
| invop[a] | 537 | 201 | | 15% | | 5 - 15 | 1.953 | 2.1 | 5.1 |
| wdp | 350 | | | | 6 | 8 - 20 | 0.7[b] | 2.1 | 5.3 |
| nrPC | 300 | 75 | | 20% | | 6 - 12 | 1.3 | 2.0 | 5.8 |
| scPore[c] | 350 | 200 | $r$ | 66% | | | 1.3 | 4.0 | 5.9 |

[a]Results of invop-MR are from Ref. [49] for center-to-center opal distance $D = 380$ nm and $n_L = 6$, where $r$ is the radius of the opal sphere. The optimization on $F$ for invop-FS architecture is discussed in Appendix B.2.
[b]Here $n_L = 4$ and $F = 50\%$ is taken as an example due to its facile fabrication.
[c]The MAPD increases to 7.65 mA cm$^{-2}$ for a 10 $\mu$m-thick scPore with also optimized $r = 175$ nm ($F = 74\%$) [58].

The inverse opals (invop) are useful for low-cost, low-efficiency photocatalysis without long-distance charge transport, such as large-scale environmental remediation applications. In the past, slow-light modes on the edges of the fundamental stop gap of invops have been utilized. Higher quality invops with sphere diameter $\sim 350$ nm improve the photocatalytic efficiency considerably by trapping sunlight in the higher-order slow-light photonic bands 5 to 15.

The simple cubic woodpiles (wdp) may be suitable for small-scale, high-efficiency photocatalysis using the experimentally demonstrated higher-order photonic bands. The charge conduction paths are much shorter and more straightforward than in invops, reducing the carrier recombinations.

The optimized nanorod array (nrPC) and slanted conical-pore (scPore) PCs strongly reduce incident light reflectivity and enhance light absorptivity. Both facilitate excellent charge transport, offering unobstructed conduction paths to the catalyst-electrolyte interface and the back contact. Photogenerated holes with short diffusion length can reach the catalyst-electrolyte interface by diffusing a distance less than one lattice constant ($\sim 350$ nm), while photogenerated electrons with long diffusion length can be collected at the bottom of the PC after traveling a distance on the order of the PC thickness. Such bifurcation of the minority and majority carrier flow,

Optics EXPRESS

together with the light trapping capability, makes these two structures suitable for high-efficiency photocatalysis and solar fuel generation by water splitting. The optimized scPore is superior to the nrPC since it traps sunlight even more effectively and enables excellent charge transport. For lightly doped $TiO_2$ with imaginary part of the sub-gap dielectric constant 0.01, the MAPD reaches 4 mA cm$^{-2}$ in 1.3 $\mu$m-thick scPore of 66.1% filling fraction on perfect mirror substrate. This increases to 7.65 mA cm$^{-2}$ with 10 $\mu$m thickness of 74% $TiO_2$ filling fraction (see Table 1).

Of the four PCs studied, the scPore emerges as the best overall architecture for solar energy harvesting through a combination of best antireflection behaviour, best light trapping, and straightforward charge carrier transport.

Photocatalysis involves carrier photogeneration, electron and hole transports in the bulk, and charge transfer at the catalyst-electrolyte interface. In this work, we primarily focus on the the significant improvement in photogeneration by optimized solar light trapping in PCs. Future investigation may combine optimized light trapping with comprehensive and microscopic modeling of bulk and interfacial charge carrier dynamics. This requires further detailed experimental measurements of key parameters such as surface recombination velocity of charges at the interface between lightly doped $TiO_2$ and aqueous solution. We hope our findings will stimulate more focused experimental studies on efficient photocatalysis based on optimized photonic crystals.

## Appendix A. Dispersive dielectric model of anatase $TiO_2$

We characterize the optical properties of anatase by a Lorentz model of the dielectric function

$$\varepsilon(\omega) = \varepsilon_\infty + \sum_n \frac{s_n \omega_n^2}{\omega_n^2 - \omega^2 - i\omega\gamma_n}, \tag{5}$$

where $\varepsilon = \varepsilon' + i\varepsilon''$, $\omega$ is the frequency of incident light, $\varepsilon_\infty$ is a real constant number equal to $\varepsilon'$ at the infinite frequency, $\omega_n$ and $\gamma_n$ are the resonance frequency and width of the $n$th Lorentz oscillator, respectively, and the dimensionless real number $s_n$ specifies the strength of the $n$th resonance.

The dispersive dielectric Model II of $TiO_2$ is obtained by fitting the experimental data reported in the early work on optical properties of single crystalline anatase [54]. The imaginary parts of

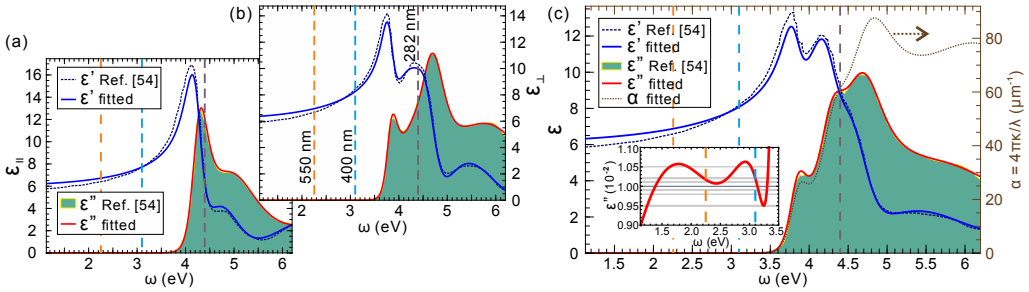


**Fig. 8.** Dielectric Model II of lightly doped anatase $TiO_2$. The deep violet dashed lines and green filled yellow lines correspond to the experimental data fetched from Ref. [54], and the solid blue and red lines are the fitted analytical curves of dielectric functions using Lorentz model (5) and Table 2 for electric fields (a) parallel and (b) perpendicular to the optical axis of single crystalline anatase. (c) The dielectric function of polycrystalline anatase is taken to be the weighted average of $\varepsilon_\parallel$ and $\varepsilon_\perp$. The corresponding absorption coefficient $\alpha$ is also given in (c). The inset is a zoom-in of $\varepsilon''$ below 3.5 eV, with the horizontal grids marking the ±1%, 2%, and 5% variations with respect to the designated value of 0.01. The vertical purple, cyan, and orange dashed lines label the 282, 400, and 550 nm wavelengthes.

Optics EXPRESS

the dielectric functions are not available for frequencies less than ~ 3.5 eV in Ref. [54]. This is complemented with a constant $\varepsilon'' = 0.01$ to model lightly doped anatase, and fitted using Eq. (5) from 200 to 1100 nm wavelength. The fitting parameters of the dielectric functions for incident polarizations (electric field) parallel ($\varepsilon_\parallel$) and perpendicular ($\varepsilon_\perp$) to anatase optical axis are given in Table 2, and the fitting result is shown in Fig. 8.

**Table 2. Fitting parameters of the dielectric function for lightly doped single crystalline anatase $TiO_2$ in Ref. [54] using Lorentz model (5).**

| | $\varepsilon_\infty$ | $n$ | $s_n$ | $\omega_n$ (eV) | $\gamma_n$ (eV) |
|---|---|---|---|---|---|
| $\varepsilon_\parallel$ | 3.575772 | 1 | 3.484559 | 4.28117418 | 0.54553045 |
| | | 2 | −2.208034 | 4.87629831 | 2.38545587 |
| | | 3 | 0.846480 | 7.37210011 | 1.81760827 |
| | | 4 | 3.289875 | 5.00524187 | 1.57459925 |
| | | 5 | −2.876320 | 4.22042193 | 0.67695369 |
| $\varepsilon_\perp$ | 3.456722 | 1 | 5.126594 | 4.65932597 | 0.98691418 |
| | | 2 | 1.877224 | 5.95124126 | 2.10773128 |
| | | 3 | 1.319631 | 3.84350998 | 0.38683068 |
| | | 4 | −1.305584 | 4.51550431 | 0.67447401 |
| | | 5 | −1.112714 | 3.80011551 | 0.47361962 |
| | | 6 | −0.777115 | 4.34564596 | 3.72696484 |
| | | 7 | −1.663916 | 4.90977404 | 1.04890627 |
| | | 8 | −0.693751 | 3.94269734 | 1.42829790 |

The polycrystalline anatase dielectric function used in our FDTD simulation is assumed to be the weighted average of $\varepsilon_\parallel$ and $\varepsilon_\perp$, which is illustrated in Fig. 8(c). Depending on the sample preparation, doping strategy, and environmental temperature, polycrystalline anatase may exhibit a reduced band gap, a more gradual slope of the dielectric function at the band edge, and a moderate material dispersion in the sub-gap region. In this work we neglect these changes on the dielectric function. The inset of Fig. 8(c) shows a $\lesssim \pm 5\%$ variation of the fitted curve from the designated value of $\varepsilon'' = 0.01$ right below the band edge. Such variation is considered to be insignificant based on the smallness of the absorption coefficient.

## Appendix B. Face-centered cubic inverse opal PC

### *B.1. Structure model*

An opal PC made of close-packed, monodisperse spheres may form either face-centered cubic (fcc), hexagonal close-packed (hcp), or disordered structures. We consider, here, fcc opal configuration achieved by self-assembly of nanospheres. The densities of states for fcc and hcp inverse opals are similar [110,111]. We model the fcc opal template as composed of overlapping monodisperse, sacrificial spheres of diameter $d$ surrounding hypothetical close-packed spheres of diameter $D$. The inverse opal consists of filling the void regions with $TiO_2$ and the sacrificial spheres with aqueous solution [see Fig. 9(a)]. If $d>D$, the overlapping spheres form an interconnected network. The $TiO_2$ inverse opal has a finite thickness along its natural growth direction [111] (defined as $z$ direction) and is infinite in the $x$- and $y$-directions. The conventional fcc lattice constant is $a = \sqrt{2}D$.

The filling fraction $F$ of the inverse opal depends on the number of opal layers $n_L$ for fixed $d$ and $D$ [49]. We denote $F_{n_L}$ as the filling fraction of an $n_L$-layer invop. In Fig. 9(b) we plot the filling fractions $F$ of an 18-layer and infinite-size invops.

Optics EXPRESS

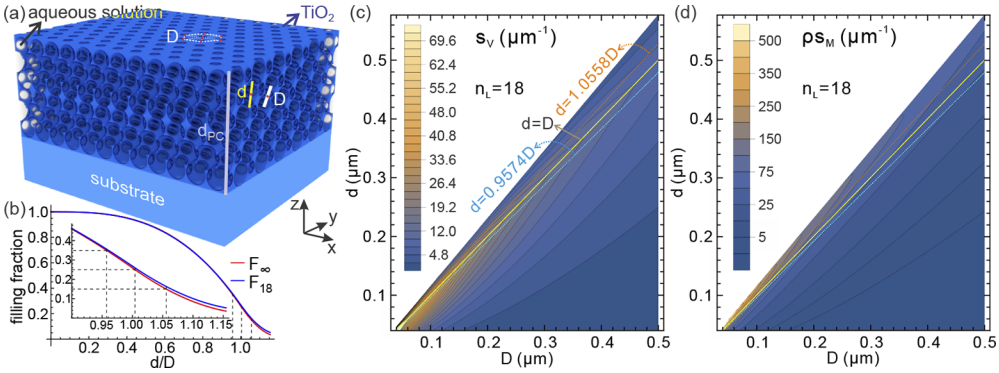


**Fig. 9.** The model of face-centered cubic inverse opal PC. (a) Illustration of $TiO_2$ 6-layer invop, with void center-to-center distance $D$ and opal sphere diameter $d$, placed on a fused silica glass or perfect mirror substrate and immersed in aqueous solution. The overall height of the PC is $d_{PC}$. (b) The filling fractions $F$ as functions of $d/D$ for invop PCs of infinite size ($n_L = \infty$) and of $n_L = 18$ opal layers. The dashed lines mark the cases of $F_\infty = 0.15$, 0.25 and 0.35, corresponding to Figs. 10(c), (d) and (e), respectively. (c, d) Color maps of the volume- and mass-specific surface areas, $s_V$ and $s_M$, respectively, of an 18-layer invop as functions of $d$ and $D$.

The volume-specific surface area for $n_L$-layer invop is

$$s_{V,n_L} = \frac{1}{D}\left[\frac{2\pi\eta^2 n_L}{\sqrt{3}\eta + \sqrt{2}\,(n_L - 1)} + \frac{1}{\eta + \frac{2}{\sqrt{6}}\,(n_L - 1)}\right], \quad \text{for } 0 \leqslant \eta \leqslant 1, \tag{6}$$

and

$$s_{V,n_L} = \frac{1}{D}\left\{\frac{2\pi\eta^2\left[n_L\left(\frac{6}{\eta} - 5\right) + 3\left(1 - \frac{1}{\eta}\right)\right]}{\sqrt{3}\eta + \sqrt{2}\,(n_L - 1)} + \frac{1}{\eta + \frac{2}{\sqrt{6}}\,(n_L - 1)}\right\}, \quad \text{for } 1 \leqslant \eta \leqslant \frac{2}{\sqrt{3}}, \tag{7}$$

where $\eta = d/D$. The mass-specific surface area is then given by

$$s_{M,n_L} = s_{V,n_L}/\left(\rho F_{n_L}\right), \tag{8}$$

where $\rho$ is the $TiO_2$ mass density and $F_{n_L}$ can be found in Ref. [49] ( for $\eta \in [1, 2/\sqrt{3}]$ ). In Figs. 9(c) and (d) we plot the color maps of $s_V$ and $s_M$ for an 18-layer invop as functions of $d$ and $D$, respectively.

Experimentally, invops have been fabricated in a bottom-up approach by sol-gel infiltration [112], chemical vapor deposition [102], atomic layer deposition (ALD) [113], and electrodeposition [114] into self-assembled opal templates of sphere radii 100 nm to 1 $\mu$m.

A modified Bragg formula is widely used in experiments to crudely estimate the positions of the photonic stop gaps [49]:

$$\lambda = 2\frac{d_L}{m}\sqrt{n_{\text{eff}}^2 - \sin^2\theta}, \tag{9}$$

where $d_L$ is the spacing between the structural layers, $m$ is the diffraction order, $\theta$ is the incident angle, and $n_{\text{eff}} = Fn_{TiO_2} + (1 - F)n_{H_2O}$ is an effective refractive index, where $F$ is the filling fraction of $TiO_2$, $n_{TiO_2}$ and $n_{H_2O}$ are the refractive indices of $TiO_2$ and water (aqueous solution), respectively. Here we consider the case of normal incidence along the [111] direction, therefore $\theta = 0$. $F$ is taken to be that of an infinite size of PC lattice along the $z$ direction.

Optics EXPRESS

### B.2. Light trapping optimization of invop PC

Previous studies of the inverse opal PC for photocatalysis have focused on slow-light modes near the edges of the fundamental optical stop gap (1st to 4th photonic bands along the Γ-L direction) [40,42]. However, the optimal slow-light modes [49] for light trapping occur between the 5th and 15th photonic bands. With opal spheres of ~ 380 nm diameter, these optimum light-trapping modes are aligned with the visible solar spectral region 400 - 550 nm.

In Ref. [49] a filling fraction $F \sim 15\%$ was assumed. For close-packed opal spheres, a complete infiltration of the voids leads to a $TiO_2$ filling fraction of 26%, for an infinite-layer invop. By depositing a conformal layer of additional sacrificial material on the opal template, air channels can be created between spherical voids after $TiO_2$ infiltration and template removal. These air channels enable a filling fraction of >60% using a secondary ALD backfilling with $TiO_2$ [113]. Here we investigate the range of experimentally accessible filling fractions from 5% to 60% [113] using the dispersionless dielectric Model I.01.

In Figs. 10(a, b) we plot $A_{avg}$ and $\beta$ for an 18-layer invop-FS architecture as functions of opal center-to-center distance $D$ and filling fraction $F$. The low values of $\beta$ along the red dashed line in Fig. 10(b) is due to strong reflection loss from the fundamental stop gap of invops. Slightly

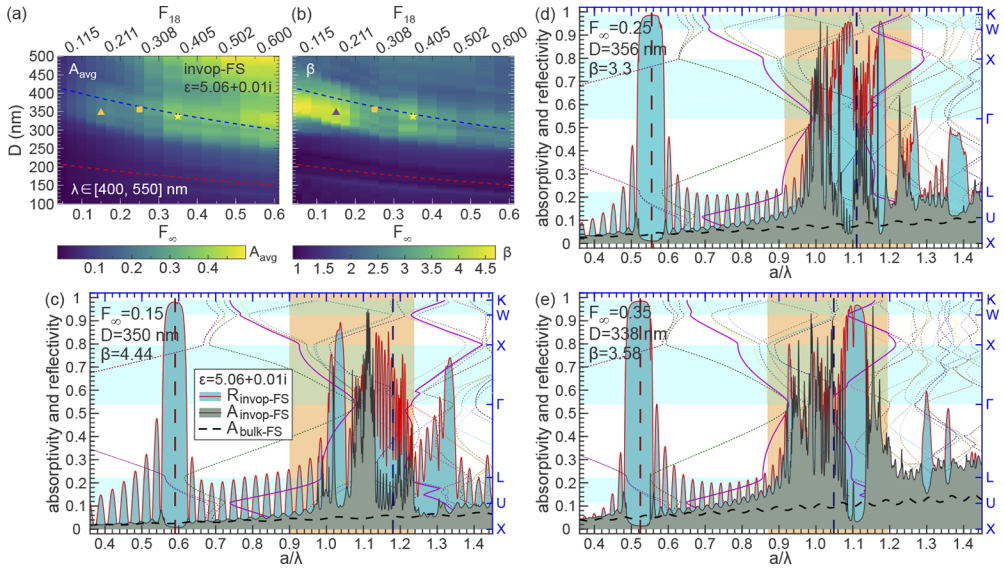


**Fig. 10.** Light trapping of face-centered cubic inverse opal PC in aqueous solution for $\lambda \in [400, 550]$ nm using the dispersionless dielectric Model I.01. (a, b) Color maps of the (a) $A_{avg}$ and (b) $\beta$ for an 18-layer invop-FS architecture as functions of opal center-to-center distance $D$ and filling fraction $F$. The red and blue dashed lines mark the contours when the first and second order Bragg reflection peaks from modified Bragg formula (9), respectively, locate at $\lambda = 463$ nm. The solid triangles, squares, and pentagrams mark the parameter sets illustrated by (c), (d), and (e), respectively. (c-e) The absorptivity (grey filled thin black lines) and reflectivity (cyan filled thin red lines) spectra of an 18-layer invop-FS architecture of (c) $F_\infty = 0.15$, (d) $F_\infty = 0.25$ and (e) $F_\infty = 0.35$. The absorptivities of bulk-FS architectures are depicted as thick black dashed lines. The background color lines depict the inverse opal band diagram, with the 5th and 15th bands highlighted. The orange shadings demark $\lambda \in [400, 550]$ nm regions in which $\beta$ is calculated. The vertical dark red and dark blue dashed lines indicate the first and second Bragg reflection peaks obtained from the modified Bragg formula (9), respectively, with $d_L = (\sqrt{6}/3)D$, $\theta = 0$, $n_{TiO_2} = 2.25$, $n_{H_2O} = 1.33$, and $F = F_\infty$. The frequency is given in terms of $a/\lambda$, where $a = \sqrt{2}D$ is the lattice constant.

Optics EXPRESS

below and above the red dashed line, a small improvement occurs due to the red- and blue-edge slow-light modes, respectively. Figures 10(a) and (b) reveal that far superior light absorption is enabled by using larger opal spheres that place higher order slow-light modes into the 400 - 550 nm range.

Increasing the filling fraction of $TiO_2$ in the PC enhances the average absorptivity but reduces the enhancement factor $\beta$. It also shifts all photonic bands to lower frequency [see Figs. 10(c-e)]. As a result, the optimum value of $D$, placing the higher-order slow-light modes in $\lambda \in [400, 550]$ nm region, becomes smaller for larger $F$, as shown in Figs. 10(a, b). $F \sim 15\%$ [Fig. 10(c)] is an optimum filling fraction in terms of absorption enhancement. $F \sim 35\%$ [Fig. 10(e)] also shows a rise of $\beta$. However, the fabrication of the invop with $F \sim 35\%$ involves a more complicated process of secondary back-filling with $TiO_2$ after the original sacrificial template is removed.

In Figs. 10(c-e) we show the absorptivity and reflectivity spectra of an 18-layer invop-FS architecture with $F_{18} = 16.3\%$ ($F_\infty = 15\%$, $D = 350$ nm, $d = 369.5$ nm), $F_{18} = 25.9\%$ ($F_\infty = 25\%$, $D = 356$ nm, $d = 357.5$ nm), and $F_{18} = 35.6\%$ ($F_\infty = 35\%$, $D = 338$ nm, $d = 323.6$ nm). Around the fundamental stop gap, the absorptivity of red-edge slow-light is slightly higher than that of the blue-edge. The slow-light modes between bands 5 to 15 exhibit superior light trapping than either edge of the fundamental stop gap. When these higher-order photonic modes are placed into the spectral region of $\lambda \in [400, 550]$ nm, the inverse opal with optimum filling fractions of $F_\infty = 15\%$ [Fig. 10(c)] demonstrates an average absorptivity enhancement factor of 4.44, while that with $F_\infty = 35\%$ [Fig. 10(e)] demonstrates $\beta = 3.58$. Figure 10 also reveals the actual location of the "second-order reflection" peak. This reflection peak is not accurately predicted by the modified Bragg formula (9), as seen by the dark blue dashed line in Fig. 10(e).

## Appendix C. Structure model of slanted conical-pore PC

A right cone with base radius $r$, height $h$ and apex P is depicted in Fig. 11(a). The corresponding slanted cone, or oblique cone, is obtained by shifting the apex P, in the positive $x$ direction, by the slant distance $p$. For numerical purposes we model the slanted cone by a stack of very thin cylinders, each with a height of one FDTD mesh size (i.e., $a/70$ where $a$ is the lattice constant). The elementary cylinder at the vertical position $z$ centering at $((1 - z/h)p, 0, z)$ has radius $(r/h)z$. The scPore PC is obtained by filling all regions exterior to a square lattice array of such cones, with $TiO_2$ and interior regions with aqueous solution. In this work we mainly discuss the case

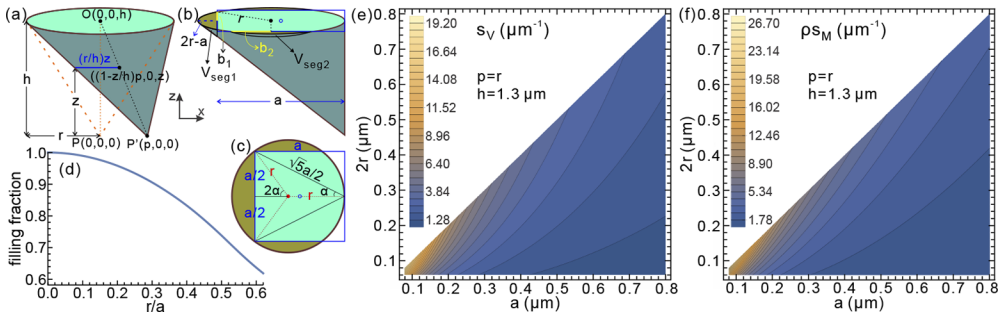


**Fig. 11.** The model of the square lattice slanted conical-pore PC. (a) A general slanted cone is modeled as a stack of elementary cylinders with radii and centers changing with z. (b) The chosen PC unit cell cuts off three segment cones from each slanted cone, one with volume $V_{seg1}$ (half-base $b_1$) and two with volumes $V_{seg2}$ (half-bases $b_2$). (c) Top view of the slanted cone and PC unit cell when $r/a = 5/8$. (d) The $TiO_2$ filling fraction as a function of $r/a$ of an scPore PC. (e, f) Color maps of the volume- and mass-specific surface areas of a 1.3 $\mu$m-thick scPore PC as functions of 2r and a for $r/a \leqslant 1/2$.

Optics EXPRESS

of $p = r$, with the vertical side of the slanted cone aligned to one side of the PC unit cell [see Figs. 11(b) and (c)]. The height of the PC is $h$.

The $TiO_2$ filling fraction of such an scPore PC depends on the relative size of the base radius $r$ and the lattice constant $a$. When $r \leqslant a/2$, each slanted cone has a volume of $(1/3)\pi r^2 h$, and the filling fraction of the PC is simply $F = 1 - (1/3)\pi(r/a)^2$. When $a/2 \leqslant r \leqslant (5/8)a$, the PC unit cell cuts off three disconnected "segment cones" from the the slanted cone [as illustrated in Fig. 11(b)] which needs to be taken into account for the $TiO_2$ volume fraction. The resulting filling fraction $F$ for $r \leqslant (5/8)a$ depends only on the ratio of $r/a$. In Fig. 11(d) the filling fraction $F$ is plotted as a function of $r/a$ for $r/a \leqslant 5/8$.

It is straightforward to obtain the lateral surface area of a single, isolated, intact slanted cone:

$$S_{\text{lateral}} = \frac{r}{2}\int_0^{2\pi} \sqrt{h^2 + (r - p\sin\theta)^2}\, d\theta. \tag{10}$$

For the sake of simplicity we consider only the case of $2r \leqslant a$. Then the total surface area is the sum of the lateral and top surface areas $S_{\text{tot}} = S_{\text{lateral}} + a^2 - \pi r^2$. The volume-specific surface area is $s_V = S_{\text{tot}}/(a^2 h)$, and the mass-specific surface area is $s_M = S_{\text{tot}}/(a^2 h \rho F)$ where $\rho$ is the $TiO_2$ mass density and $F$ is the filling fraction. In Figs. 11(e) and (f) we plot the color maps of $s_V$ and $s_M$ of an scPore PC with $h = 1.3$ $\mu$m for $r \leqslant a/2$.

**Funding.** Ontario Research Fund; Natural Sciences and Engineering Research Council of Canada.

**Acknowledgments.** We are grateful to Wojciech Macyk, Shawn-Yu Lin, Joanna Kuncewicz, Paulina O'Callaghan and Brian Frey for useful discussions.

**Disclosures.** The authors declare no conflicts of interest.

**Data availability.** Data underlying the results presented in this paper are not publicly available at this time but may be obtained from the authors upon reasonable request.

## References

1. A. Fujishima, X. Zhang, and D. A. Tryk, "$TiO_2$ photocatalysis and related surface phenomena," Surf. Sci. Rep. **63**(12), 515–582 (2008).
2. J. Schneider, M. Matsuoka, M. Takeuchi, J. Zhang, Y. Horiuchi, M. Anpo, and D. W. Bahnemann, "Understanding $TiO_2$ photocatalysis: Mechanisms and materials," Chem. Rev. **114**(19), 9919–9986 (2014).
3. O. K. Varghese, D. Gong, M. Paulose, K. G. Ong, E. C. Dickey, and C. A. Grimes, "Extreme changes in the electrical resistance of titania nanotubes with hydrogen exposure," Adv. Mater. **15**(78), 624–627 (2003).
4. B. O'Regan and M. Grätzel, "A low-cost, high-efficiency solar cell based on dye-sensitized colloidal $TiO_2$ films," Nature **353**(6346), 737–740 (1991).
5. M. Möller, S. Asaftei, D. Corr, M. Ryan, and L. Walder, "Switchable electrochromic images based on a combined top–down bottom–up approach," Adv. Mater. **16**(17), 1558–1562 (2004).
6. J.-K. Lee, D.-S. Choi, I. Jang, and W.-Y. Choi, "Improved osseointegration of dental titanium implants by $TiO_2$ nanotube arrays with recombinant human bone morphogenetic protein-2: a pilot in vivo study," Int. J. Nanomed. **10**, 1145–1154 (2015).
7. A. Fujishima and K. Honda, "Electrochemical photolysis of water at a semiconductor electrode," Nature **238**(5358), 37–38 (1972).
8. A. J. Nozik, "Photoelectrolysis of water using semiconducting $TiO_2$ crystals," Nature **257**(5525), 383–386 (1975).
9. M. R. Hoffmann, S. T. Martin, W. Choi, and D. W. Bahnemann, "Environmental applications of semiconductor photocatalysis," Chem. Rev. **95**(1), 69–96 (1995).
10. J. C. Yu, W. Ho, J. Yu, H. Yip, P. K. Wong, and J. Zhao, "Efficient visible-light-induced photocatalytic disinfection on sulfur-doped nanocrystalline titania," Environ. Sci. Technol. **39**(4), 1175–1179 (2005).
11. T. Rajh, N. M. Dimitrijevic, M. Bissonnette, T. Koritarov, and V. Konda, "Titanium dioxide in the service of the biomedical revolution," Chem. Rev. **114**(19), 10177–10216 (2014).
12. A. Sarkar and G. G. Khan, "The formation and detection techniques of oxygen vacancies in titanium oxide-based nanostructures," Nanoscale **11**(8), 3414–3444 (2019).
13. R. Sanjinés, H. Tang, H. Berger, F. Gozzo, G. Margaritondo, and F. Lévy, "Electronic structure of anatase $TiO_2$ oxide," J. Appl. Phys. **75**(6), 2945–2951 (1994).
14. A. G. Thomas, W. R. Flavell, A. R. Kumarasinghe, A. K. Mallick, D. Tsoutsou, G. C. Smith, R. Stockbauer, S. Patel, M. Grätzel, and R. Hengerer, "Resonant photoemission of anatase $TiO_2$ (101) and (001) single crystals," Phys. Rev. B **67**(3), 035110 (2003).

Optics EXPRESS


15. F. De Angelis, C. Di Valentin, S. Fantacci, A. Vittadini, and A. Selloni, "Theoretical studies on anatase and less common $TiO_2$ phases: bulk, surfaces, and nanomaterials," Chem. Rev. **114**(19), 9708–9753 (2014).
16. T.-H. Xie and J. Lin, "Origin of photocatalytic deactivation of $TiO_2$ film coated on ceramic substrate," J. Phys. Chem. C **111**(27), 9968–9974 (2007).
17. X. Pan, N. Zhang, X. Fu, and Y.-J. Xu, "Selective oxidation of benzyl alcohol over $TiO_2$ nanosheets with exposed {001} facets: catalyst deactivation and regeneration," Appl. Catal. A **453**, 181–187 (2013).
18. F. Zuo, L. Wang, T. Wu, Z. Zhang, D. Borchardt, and P. Feng, "Self-doped $Ti^{3+}$ enhanced photocatalyst for hydrogen production under visible light," J. Am. Chem. Soc. **132**(34), 11856–11857 (2010).
19. D. Qi, L. Lu, Z. Xi, L. Wang, and J. Zhang, "Enhanced photocatalytic performance of $TiO_2$ based on synergistic effect of $Ti^{3+}$ self-doping and slow light effect," Appl. Catal. B **160-161**, 621–628 (2014).
20. W. Choi, A. Termin, and M. R. Hoffmann, "The role of metal ion dopants in quantum-sized $TiO_2$: correlation between photoreactivity and charge carrier recombination dynamics," J. Phys. Chem. **98**(51), 13669–13679 (1994).
21. Q. Wang and K. Domen, "Particulate photocatalysts for light-driven water splitting: mechanisms, challenges, and design strategies," Chem. Rev. **120**(2), 919–985 (2020).
22. W. Zhu, X. Qiu, V. Iancu, X.-Q. Chen, H. Pan, W. Wang, N. M. Dimitrijevic, T. Rajh, H. M. Meyer III, M. P. Paranthaman, G. M. Stocks, H. H. Weitering, B. Gu, G. Eres, and Z. Zhang, "Band gap narrowing of titanium oxide semiconductors by noncompensated anion-cation codoping for enhanced visible-light photoactivity," Phys. Rev. Lett. **103**(22), 226401 (2009).
23. Y. Gai, J. Li, S.-S. Li, J.-B. Xia, and S.-H. Wei, "Design of narrow-gap $TiO_2$: a passivated codoping approach for enhanced photoelectrochemical activity," Phys. Rev. Lett. **102**(3), 036402 (2009).
24. X. Chen, L. Liu, P. Y. Yu, and S. S. Mao, "Increasing solar absorption for photocatalysis with black hydrogenated titanium dioxide nanocrystals," Science **331**(6018), 746–750 (2011).
25. J. Cai, M. Wu, Y. Wang, H. Zhang, M. Meng, Y. Tian, X. Li, J. Zhang, L. Zheng, and J. Gong, "Synergetic enhancement of light harvesting and charge separation over surface-disorder-engineered $TiO_2$ photonic crystals," Chem **2**(6), 877–892 (2017).
26. M. K. Nowotny, L. R. Sheppard, T. Bak, and J. Nowotny, "Defect chemistry of titanium dioxide. application of defect engineering in processing of $TiO_2$-based photocatalysts," J. Phys. Chem. C **112**(14), 5275–5300 (2008).
27. B. A. D. Williamson, J. Buckeridge, N. P. Chadwick, S. Sathasivam, C. J. Carmalt, I. P. Parkin, and D. O. Scanlon, "Dispelling the myth of passivated codoping in $TiO_2$," Chem. Mater. **31**(7), 2577–2589 (2019).
28. M. Radecka, M. Rekas, A. Trenczek-Zajac, and K. Zakrzewska, "Importance of the band gap energy and flat band potential for application of modified $TiO_2$ photoanodes in water photolysis," J. Power Sources **181**(1), 46–55 (2008).
29. S. N. R. Inturi, T. Boningari, M. Suidan, and P. G. Smirniotis, "Visible-light-induced photodegradation of gas phase acetonitrile using aerosol-made transition metal (V, Cr, Fe, Co, Mn, Mo, Ni, Cu, Y, Ce, and Zr) doped $TiO_2$," Appl. Catal. B **144**, 333–342 (2014).
30. Y. Tian and T. Tatsuma, "Mechanisms and applications of plasmon-induced charge separation at $TiO_2$ films loaded with gold nanoparticles," J. Am. Chem. Soc. **127**(20), 7632–7637 (2005).
31. S. Mubeen, J. Lee, N. Singh, S. Krämer, G. D. Stucky, and M. Moskovits, "An autonomous photosynthetic device in which all charge carriers derive from surface plasmons," Nat. Nanotechnol. **8**(4), 247–251 (2013).
32. P. Wang, B. Huang, Y. Dai, and M.-H. Whangbo, "Plasmonic photocatalysts: harvesting visible light with noble metal nanoparticles," Phys. Chem. Chem. Phys. **14**(28), 9813–9825 (2012).
33. A. Furube, L. Du, K. Hara, R. Katoh, and M. Tachiya, "Ultrafast plasmon-induced electron transfer from gold nanodots into $TiO_2$ nanoparticles," J. Am. Chem. Soc. **129**(48), 14852–14853 (2007).
34. C. Gomes Silva, R. Juárez, T. Marino, R. Molinari, and H. García, "Influence of excitation wavelength (UV or visible light) on the photocatalytic activity of titania containing gold nanoparticles for the generation of hydrogen or oxygen from water," J. Am. Chem. Soc. **133**(3), 595–602 (2011).
35. J. B. Priebe, M. Karnahl, H. Junge, M. Beller, D. Hollmann, and A. Brückner, "Water reduction with visible light: synergy between optical transitions and electron transfer in Au-$TiO_2$ catalysts visualized by in situ EPR spectroscopy," Angew. Chem. Int. Ed. **52**(43), 11420–11424 (2013).
36. E. Kazuma and T. Tatsuma, "In situ nanoimaging of photoinduced charge separation at the plasmonic au nanoparticle-$TiO_2$ interface," Adv. Mater. Interfaces **1**(3), 1400066 (2014).
37. L. Du, A. Furube, K. Yamamoto, K. Hara, R. Katoh, and M. Tachiya, "Plasmon-induced charge separation and recombination dynamics in gold-$TiO_2$ nanoparticle systems: dependence on $TiO_2$ particle size," J. Phys. Chem. C **113**(16), 6454–6462 (2009).
38. W. Hou and S. B. Cronin, "A review of surface plasmon resonance-enhanced photocatalysis," Adv. Funct. Mater. **23**(13), 1612–1619 (2013).
39. S. John, "Strong localization of photons in certain disordered dielectric superlattices," Phys. Rev. Lett. **58**(23), 2486–2489 (1987).
40. J. I. L. Chen, G. von Freymann, S. Y. Choi, V. Kitaev, and G. A. Ozin, "Amplified photochemistry with slow photons," Adv. Mater. **18**(14), 1915–1919 (2006).
41. Y. Z. Li, T. Kunitake, and S. Fujikawa, "Efficient fabrication and enhanced photocatalytic activities of 3D-ordered films of titania hollow spheres," J. Phys. Chem. B **110**(26), 13000–13004 (2006).
42. V. Likodimos, "Photonic crystal-assisted visible light activated $TiO_2$ photocatalysis," Appl. Catal. B **230**, 269–303 (2018).

Optics EXPRESS


43. B. J. Frey, P. Kuang, M.-L. Hsieh, J.-H. Jiang, S. John, and S.-Y. Lin, "Effectively infinite optical path-length created using a simple cubic photonic crystal for extreme light trapping," Sci. Rep. **7**(1), 4171 (2017).
44. J. I. L. Chen, G. von Freymann, S. Y. Choi, V. Kitaev, and G. A. Ozin, "Slow photons in the fast lane in chemistry," J. Mater. Chem. **18**(4), 369–373 (2008).
45. Y. Lu, H. Yu, S. Chen, X. Quan, and H. Zhao, "Integrating plasmonic nanoparticles with $TiO_2$ photonic crystal for enhancement of visible-light-driven photocatalysis," Environ. Sci. Technol. **46**(3), 1724–1730 (2012).
46. C. Cheng, S. K. Karuturi, L. Liu, J. Liu, H. Li, L. T. Su, A. I. Y. Tok, and H. J. Fan, "Quantum-dot-sensitized $TiO_2$ inverse opals for photoelectrochemical hydrogen generation," Small **8**(1), 37–42 (2012).
47. M. Curti, J. Schneider, D. W. Bahnemann, and C. B. Mendive, "Inverse opal photonic crystals as a strategy to improve photocatalysis: underexplored questions," J. Phys. Chem. Lett. **6**(19), 3903–3910 (2015).
48. O. Deparis, S. R. Mouchet, and B.-L. Su, "Light harvesting in photonic crystals revisited: why do slow photons at the blue edge enhance absorption?" Phys. Chem. Chem. Phys. **17**(45), 30525–30532 (2015).
49. X. Zhang and S. John, "Enhanced photocatalysis by light-trapping optimization in inverse opals," J. Mater. Chem. A **8**(36), 18974–18986 (2020).
50. S. Y. Lin, J. G. Fleming, D. L. Hetherington, B. K. Smith, R. Biswas, K. M. Ho, M. M. Sigalas, W. Zubrzycki, S. R. Kurtz, and J. Bur, "A three-dimensional photonic crystal operating at infrared wavelengths," Nature **394**(6690), 251–253 (1998).
51. J. Augustynski, "The role of the surface intermediates in the photoelectrochemical behaviour of anatase and rutile $TiO_2$," Electrochim. Acta **38**(1), 43–46 (1993).
52. T. Sekiya, T. Yagisawa, N. Kamiya, D. Das Mulmi, S. Kurita, Y. Murakami, and T. Kodaira, "Defects in anatase $TiO_2$ single crystal controlled by heat treatments," J. Phys. Soc. Jpn. **73**(3), 703–710 (2004).
53. D. Mardare and P. Hones, "Optical dispersion analysis of $TiO_2$ thin films based on variable-angle spectroscopic ellipsometry measurements," Mater. Sci. Eng., B **68**(1), 42–47 (1999).
54. N. Hosaka, T. Sekiya, C. Satoko, and S. Kurita, "Optical properties of single-crystal anatase $TiO_2$," J. Phys. Soc. Jpn. **66**(3), 877–880 (1997).
55. H. Tang, F. Lévy, H. Berger, and P. E. Schmid, "Urbach tail of anatase $TiO_2$," Phys. Rev. B **52**(11), 7771–7774 (1995).
56. G. E. Jellison, L. A. Boatner, J. D. Budai, B.-S. Jeong, and D. P. Norton, "Spectroscopic ellipsometry of thin film and bulk anatase ($TiO_2$)," J. Appl. Phys. **93**(12), 9537–9541 (2003).
57. E. Baldini, L. Chiodo, A. Dominguez, M. Palummo, S. Moser, M. Yazdi-Rizi, G. Auböck, B. P. P. Mallett, H. Berger, A. Magrez, C. Bernhard, M. Grioni, A. Rubio, and M. Chergui, "Strongly bound excitons in anatase $TiO_2$ single crystals and nanoparticles," Nat. Commun. **8**(1), 13 (2017).
58. X. Zhang and S. John, "Photonic crystal based photoelectrochemical cell for solar fuels," Nano Select **2**(6), 1218–1224 (2021).
59. W. H. Leng, P. R. F. Barnes, M. Juozapavicius, B. C. O'Regan, and J. R. Durrant, "Electron diffusion length in mesoporous nanocrystalline $TiO_2$ photoelectrodes during water oxidation," J. Phys. Chem. Lett. **1**(6), 967–972 (2010).
60. S. Wong, M. Deubel, F. Pérez-Willard, S. John, G. A. Ozin, M. Wegener, and G. von Freymann, "Direct laser writing of three-dimensional photonic crystals with a complete photonic bandgap in chalcogenide glasses," Adv. Mater. **18**(3), 265–269 (2006).
61. G. M. Gratson, M. Xu, and J. A. Lewis, "Direct writing of three-dimensional webs," Nature **428**(6981), 386 (2004).
62. A. Chutinan and S. John, "Light trapping and absorption optimization in certain thin-film photonic crystal architectures," Phys. Rev. A **78**(2), 023825 (2008).
63. G. Demésy and S. John, "Solar energy trapping with modulated silicon nanowire photonic crystals," J. Appl. Phys. **112**(7), 074326 (2012).
64. P. Kuang, A. Deinega, M.-L. Hsieh, S. John, and S.-Y. Lin, "Light trapping and near-unity solar absorption in a three-dimensional photonic-crystal," Opt. Lett. **38**(20), 4200–4203 (2013).
65. S. Foster and S. John, "Light-trapping in dye-sensitized solar cells," Energy Environ. Sci. **6**(10), 2972–2983 (2013).
66. X. Zhang and S. John, "Broadband light-trapping enhancement of graphene absorptivity," Phys. Rev. B **99**(3), 035417 (2019).
67. A. I. Hochbaum and P. Yang, "Semiconductor nanowires for energy conversion," Chem. Rev. **110**(1), 527–546 (2010).
68. K. T. Fountaine, W. S. Whitney, and H. A. Atwater, "Resonant absorption in semiconductor nanowires and nanowire arrays: relating leaky waveguide modes to Bloch photonic crystal modes," J. Appl. Phys. **116**(15), 153106 (2014).
69. N. Dhindsa and S. S. Saini, "Comparison of ordered and disordered silicon nanowire arrays: experimental evidence of photonic crystal modes," Opt. Lett. **41**(9), 2045–2048 (2016).
70. L. Hu and G. Chen, "Analysis of optical absorption in silicon nanowire arrays for photovoltaic applications," Nano Lett. **7**(11), 3249–3252 (2007).
71. C. Lin and M. L. Povinelli, "Optical absorption enhancement in silicon nanowire arrays with a large lattice constant for photovoltaic applications," Opt. Express **17**(22), 19371–19381 (2009).
72. B. C. P. Sturmberg, K. B. Dossou, L. C. Botten, A. A. Asatryan, C. G. Poulton, C. M. de Sterke, and R. C. McPhedran, "Modal analysis of enhanced absorption in silicon nanowire arrays," Opt. Express **19**(S5), A1067–A1081 (2011).
73. N. Huang, C. Lin, and M. L. Povinelli, "Broadband absorption of semiconductor nanowire arrays for photovoltaic applications," J. Opt. **14**(2), 024004 (2012).

Optics EXPRESS


74. N. Dhindsa, R. Kohandani, and S. S. Saini, "Length dependent optical characteristics analysis for semiconductor nanowires," Nanotechnology **31**(22), 224001 (2020).
75. J. Kupec, R. L. Stoop, and B. Witzigmann, "Light absorption and emission in nanowire array solar cells," Opt. Express **18**(26), 27589–27605 (2010).
76. L. Wen, Z. Zhao, X. Li, Y. Shen, H. Guo, and Y. Wang, "Theoretical analysis and modeling of light trapping in high efficicency GaAs nanowire array solar cells," Appl. Phys. Lett. **99**(14), 143116 (2011).
77. Z. Wang, D. Cao, R. Xu, S. Qu, Z. Wang, and Y. Lei, "Realizing ordered arrays of nanostructures: a versatile platform for converting and storing energy efficiently," Nano Energy **19**, 328–362 (2016).
78. J. Zhu, Z. Yu, G. F. Burkhard, C.-M. Hsu, S. T. Connor, Y. Xu, Q. Wang, M. McGehee, S. Fan, and Y. Cui, "Optical absorption enhancement in amorphous silicon nanowire and nanocone arrays," Nano Lett. **9**(1), 279–282 (2009).
79. E. Garnett and P. Yang, "Light trapping in silicon nanowire solar cells," Nano Lett. **10**(3), 1082–1087 (2010).
80. M. D. Kelzenberg, S. W. Boettcher, J. A. Petykiewicz, D. B. Turner-Evans, M. C. Putnam, E. L. Warren, J. M. Spurgeon, R. M. Briggs, N. S. Lewis, and H. A. Atwater, "Enhanced absorption and carrier collection in Si wire arrays for photovoltaic applications," Nat. Mater. **9**(3), 239–244 (2010).
81. Z. Fan, R. Kapadia, P. W. Leu, X. Zhang, Y.-L. Chueh, K. Takei, K. Yu, A. Jamshidi, A. A. Rathore, D. J. Ruebusch, M. Wu, and A. Javey, "Ordered arrays of dual-diameter nanopillars for maximized optical absorption," Nano Lett. **10**(10), 3823–3827 (2010).
82. Q. Li, K. R. Westlake, M. H. Crawford, S. R. Lee, D. D. Koleske, J. J. Figiel, K. C. Cross, S. Fathololoumi, Z. Mi, and G. T. Wang, "Optical performance of top-down fabricated InGaN/GaN nanorod light emitting diode arrays," Opt. Express **19**(25), 25528–25534 (2011).
83. L. E. Jensen, M. T. Björk, S. Jeppesen, A. I. Persson, B. J. Ohlsson, and L. Samuelson, "Role of surface diffusion in chemical beam epitaxy of inas nanowires," Nano Lett. **4**(10), 1961–1964 (2004).
84. S. L. Diedenhofen, O. T. A. Janssen, G. Grzela, E. P. A. M. Bakkers, and J. Gómez Rivas, "Strong geometrical dependence of the absorption of light in arrays of semiconductor nanowires," ACS Nano **5**(3), 2316–2323 (2011).
85. X. Zhang, D. Liu, L. Zhang, W. Li, M. Gao, W. Ma, Y. Ren, Q. Zeng, Z. Niu, W. Zhou, and S. Xie, "Synthesis of large-scale periodic ZnO nanorod arrays and its blue-shift of UV luminescence," J. Mater. Chem. **19**(7), 962–969 (2009).
86. B. Liu and E. S. Aydil, "Growth of oriented single-crystalline rutile $TiO_2$ nanorods on transparent conducting substrates for dye-sensitized solar cells," J. Am. Chem. Soc. **131**(11), 3985–3990 (2009).
87. G. Wang, H. Wang, Y. Ling, Y. Tang, X. Yang, R. C. Fitzmorris, C. Wang, J. Z. Zhang, and Y. Li, "Hydrogen-treated $TiO_2$ nanowire arrays for photoelectrochemical water splitting," Nano Lett. **11**(7), 3026–3033 (2011).
88. C. A. Chen, Y. M. Chen, A. Korotcov, Y. S. Huang, D. S. Tsai, and K. K. Tiong, "Growth and characterization of well-aligned densely-packed rutile $TiO_2$ nanocrystals on sapphire substrates via metal–organic chemical vapor deposition," Nanotechnology **19**(7), 075611 (2008).
89. Y. Lei, L. D. Zhang, G. W. Meng, G. H. Li, X. Y. Zhang, C. H. Liang, W. Chen, and S. X. Wang, "Preparation and photoluminescence of highly ordered $TiO_2$ nanowire arrays," Appl. Phys. Lett. **78**(8), 1125–1127 (2001).
90. Y. Li, T. Sasaki, Y. Shimizu, and N. Koshizaki, "Hexagonal-close-packed, hierarchical amorphous $TiO_2$ nanocolumn arrays: transferability, enhanced photocatalytic activity, and superamphiphilicity without UV irradiation," J. Am. Chem. Soc. **130**(44), 14755–14762 (2008).
91. P. Shi, X. Li, Q. Zhang, Z. Yi, and J. Luo, "Photocatalytic activity of self-assembled porous $TiO_2$ nano-columns array fabricated by oblique angle sputter deposition," Mater. Res. Express **5**(4), 045018 (2018).
92. H. Masuda, K. Kanezawa, M. Nakao, A. Yokoo, T. Tamamura, T. Sugiura, H. Minoura, and K. Nishio, "Ordered arrays of nanopillars formed by photoelectrochemical etching on directly imprinted $TiO_2$ single crystals," Adv. Mater. **15**(2), 159–161 (2003).
93. P. M. Wu, N. Anttu, H. Q. Xu, L. Samuelson, and M.-E. Pistol, "Colorful InAs nanowire arrays: from strong to weak absorption with geometrical tuning," Nano Lett. **12**(4), 1990–1995 (2012).
94. L. Li, S. Wu, Z. Zhou, P. Guo, and X. Li, "Size-dependent performances in homogeneous, controllable, and large-area silicon wire array photocathode," J. Power Sources **473**, 228580 (2020).
95. S. Eyderman, S. John, and A. Deinega, "Solar light trapping in slanted conical-pore photonic crystals: beyond statistical ray trapping," J. Appl. Phys. **113**(15), 154315 (2013).
96. A. Deinega, S. Eyderman, and S. John, "Coupled optical and electrical modeling of solar cell based on conical pore silicon photonic crystals," J. Appl. Phys. **113**(22), 224501 (2013).
97. K. Q. Le and S. John, "Synergistic plasmonic and photonic crystal light-trapping: architectures for optical up-conversion in thin-film solar cells," Opt. Express **22**(S1), A1–A12 (2014).
98. A. Mavrokefalos, S. E. Han, S. Yerci, M. S. Branham, and G. Chen, "Efficient light trapping in inverted nanopyramid thin crystalline silicon membranes for solar cell applications," Nano Lett. **12**(6), 2792–2796 (2012).
99. K. Kumar, A. Khalatpour, G. Liu, J. Nogami, and N. P. Kherani, "Converging photo-absorption limit in periodically textured ultra-thin silicon foils and wafers," Sol. Energy **155**, 1306–1312 (2017).
100. P. Kuang, S. Eyderman, M.-L. Hsieh, A. Post, S. John, and S.-Y. Lin, "Achieving an accurate surface profile of a photonic crystal for near-unity solar absorption in a super thin-film architecture," ACS Nano **10**(6), 6116–6124 (2016).
101. S. Eyderman, S. John, M. Hafez, S. S. Al-Ameer, T. S. Al-Harby, Y. Al-Hadeethi, and D. M. Bouwes, "Light-trapping optimization in wet-etched silicon photonic crystal solar cells," J. Appl. Phys. **118**(2), 023103 (2015).

Optics EXPRESS


102. A. Blanco, E. Chomski, S. Grabtchak, M. Ibisate, S. John, S. W. Leonard, C. Lopez, F. Meseguer, H. Miguez, J. P. Mondia, G. A. Ozin, O. Toader, and H. M. van Driel, "Large-scale synthesis of a silicon photonic crystal with a complete three-dimensional bandgap near 1.5 micrometres," Nature **405**(6785), 437–440 (2000).
103. A. K. Ghosh and H. P. Maruska, "Photoelectrolysis of water in sunlight with sensitized semiconductor electrodes," J. Electrochem. Soc. **124**(10), 1516–1522 (1977).
104. P. Salvador, "Hole diffusion length in n-$TiO_2$ single crystals and sintered electrodes: photoelectrochemical determination and comparative analysis," J. Appl. Phys. **55**(8), 2977–2985 (1984).
105. L. Peraldo Bicelli, G. Razzini, C. Malitesta, L. Sabbatini, and P. G. Zambonin, "Surface characterization of anodic titanium dioxide films for photoelectrochemical solar cells," Sol. Energy Mater. **13**(1), 25–35 (1986).
106. S. K. Poznyak, V. V. Sviridov, A. I. Kulak, and M. P. Samtsov, "Photoluminescence and electroluminescence at the $TiO_2$-electrolyte interface," J. Electroanal. Chem. **340**(1-2), 73–97 (1992).
107. S. K. Karuturi, C. Cheng, L. Liu, L. Tat Su, H. J. Fan, and A. I. Y. Tok, "Inverse opals coupled with nanowires as photoelectrochemical anode," Nano Energy **1**(2), 322–327 (2012).
108. C. Liu, J. Tang, H. M. Chen, B. Liu, and P. Yang, "A fully integrated nanosystem of semiconductor nanowires for direct solar water splitting," Nano Lett. **13**(6), 2989–2992 (2013).
109. N. Hayashi, K. Kato, and A. Yamakata, "Enhancement of photoelectrochemical activity of $TiO_2$ electrode by particulate/dense double-layer formation," J. Chem. Phys. **152**(24), 241101 (2020).
110. K. Busch and S. John, "Photonic band gap formation in certain self-organizing systems," Phys. Rev. E **58**(3), 3896–3908 (1998).
111. G. Subramania, K. Constant, R. Biswas, M. M. Sigalas, and K. M. Ho, "Optical photonic crystals fabricated from colloidal systems," Appl. Phys. Lett. **74**(26), 3933–3935 (1999).
112. J. E. G. J. Wijnhoven and W. L. Vos, "Preparation of photonic crystals made of air spheres in titania," Science **281**(5378), 802–804 (1998).
113. E. Graugnard, J. S. King, D. P. Gaillot, and C. J. Summers, "Sacrificial-layer atomic layer deposition for fabrication of non-close-packed inverse-opal photonic crystals," Adv. Funct. Mater. **16**(9), 1187–1196 (2006).
114. P. V. Braun and P. Wiltzius, "Electrochemical fabrication of 3D microperiodic porous materials," Adv. Mater. **13**(7), 482–485 (2001).